A divergent heritage for complex organics in Isheyevo lithic clasts

van Kooten, Elishevah M.M.E.; Nagashima, Kazuhide; Kasama, Takeshi; Wampfler, Susanne F.; Ramsey, Jon P.; Frimann, Søren; Balogh, Zoltan Imre; Schiller, Martin; Wielandt, Daniel P.; Franchi, Ian A.

Total number of authors:
13

Published in:
Geochimica et Cosmochimica Acta

Link to article, DOI:
10.1016/j.gca.2017.02.002

Publication date:
2017

Document Version
Publisher's PDF, also known as Version of record

Available online at www.sciencedirect.com

ScienceDirect

Geochimica et Cosmochimica Acta 205 (2017) 119–148

Geochimica et Cosmochimica Acta

www.elsevier.com/locate/gca

A divergent heritage for complex organics in Isheyevo lithic clasts

Elishevah M.M.E. van Kooten [a,*], Kazuhide Nagashima [b], Takeshi Kasama [c], Susanne F. Wampfler [d], Jon P. Ramsey [a,e], Søren Frimann [a,e], Zoltan I. Balogh [c], Martin Schiller [a], Daniel P. Wielandt [a], Ian A. Franchi [f], Jes K. Jørgensen [a,e], Alexander N. Krot [a,b], Martin Bizzarro [a]

[a] *Centre for Star and Planet Formation and Natural History Museum of Denmark, University of Copenhagen, DK-1350 Copenhagen, Denmark*
[b] *Hawai'i Institute of Geophysics and Planetology, University of Hawai'i at Mānoa, HI 96822, USA*
[c] *Centre for Electron Nanoscopy, Technical University of Denmark, DK-2800 Copenhagen, Denmark*
[d] *Center for Space and Habitability, University of Bern, Sidlerstrasse 5, CH-3012 Bern, Switzerland*
[e] *Niels Bohr Institute, DK-1350 Copenhagen, Denmark*
[f] *Planetary and Space Sciences, Open University, Milton Keynes MK7 6AA, UK*

Received 3 October 2016; accepted in revised form 3 February 2017; available online 16 February 2017

Abstract

Primitive meteorites are samples of asteroidal bodies that contain a high proportion of chemically complex organic matter (COM) including prebiotic molecules such as amino acids, which are thought to have been delivered to Earth via impacts during the early history of the Solar System. Thus, understanding the origin of COM, including their formation pathway (s) and environment(s), is critical to elucidate the origin of life on Earth as well as assessing the potential habitability of exoplanetary systems. The Isheyevo CH/CB$_b$ carbonaceous chondrite contains chondritic lithic clasts with variable enrichments in ^{15}N believed to be of outer Solar System origin. Using transmission electron microscopy (TEM-EELS) and *in situ* isotope analyses (SIMS and NanoSIMS), we report on the structure of the organic matter as well as the bulk H and N isotope composition of Isheyevo lithic clasts. These data are complemented by electron microprobe analyses of the clast mineral chemistry and bulk Mg and Cr isotopes obtained by inductively coupled plasma and thermal ionization mass spectrometry, respectively (MC-ICPMS and TIMS). Weakly hydrated (A) clasts largely consist of Mg-rich anhydrous silicates with local hydrated veins composed of phyllosilicates, magnetite and globular and diffuse organic matter. Extensively hydrated clasts (H) are thoroughly hydrated and contain Fe-sulfides, sometimes clustered with organic matter, as well as magnetite and carbonates embedded in a phyllosilicate matrix. The A-clasts are characterized by a more ^{15}N-rich bulk nitrogen isotope composition ($\delta^{15}N = 200–650‰$) relative to H-clasts ($\delta^{15}N = 50–180‰$) and contain extremely ^{15}N-rich domains with $\delta^{15}N < 5000‰$. The D/H ratios of the clasts are correlated with the degree of clast hydration and define two distinct populations, which we interpret as reflecting mixing between D-poor fluid(s) and distinct organic endmember components that are variably D-rich. High-resolution N isotope data of ^{15}N-rich domains show that the lithic clast diffuse organic matter is typically more ^{15}N-rich than globular organic matter. The correlated δ^{15}N values and C/N ratios of nanoglobules require the existence of multiple organic components, in agreement with the H isotope data. The combined H and N isotope data suggest that the organic precursors of the lithic clasts are defined by an extremely ^{15}N-poor (similar to solar) and D-rich component for H-clasts, and a moderately ^{15}N-rich and D-rich component for A-clasts. In contrast, the composition of the putative fluids is inferred to include D-poor but moderately to extremely ^{15}N-rich H- and N-bearing components. The variable ^{15}N enrichments in H- and A-clasts are associated with structural differences in the N bonding environments of their diffuse organic matter, which are dominated by amine groups in H-clasts and nitrile functional groups in A-clasts. We suggest that the

* Corresponding author.
E-mail address: elishevah.vankooten@snm.ku.dk (E.M.M.E. van Kooten).

http://dx.doi.org/10.1016/j.gca.2017.02.002

isotopically divergent organic precursors in Isheyevo clasts may be similar to organic moieties in carbonaceous chondrites (CI, CM, CR) and thermally recalcitrant organic compounds in ordinary chondrites, respectively. The altering fluids, which are inferred to cause the ^{15}N enrichments observed in the clasts, may be the result of accretion of variable abundances of NH_3 and HCN ices. Finally, using bulk Mg and Cr isotope composition of clasts, we speculate on the accretion regions of the various primitive chondrites and components and the origin of the Solar System's N and H isotope variability.

Keywords: Complex organic matter; Carbonaceous chondrites; Accretion regions

1. INTRODUCTION

One of the central questions regarding the formation of the Earth in the context of habitability is focused on understanding the formation region(s) of the key ingredients required for the emergence of life, namely water and complex organics molecules (COMs: molecules with six atoms or more; Herbst and Dishoeck, 2009). Some prebiotic species like the simple sugar molecule glycolaldehyde, considered to be amongst the building blocks of life, have been identified both in molecular clouds and protostellar environments (Jørgensen et al., 2012; Belloche et al., 2014) as well as in comets and samples of primitive asteroids represented by various types of chondritic meteorites (Cooper et al., 2001; Biver et al., 2015). As comets and primitive asteroids likely delivered COMs to the young Earth, understanding how these molecules were incorporated into asteroids (Bergin et al., 2015) is an important step towards elucidating the origin of life on Earth and evaluating the habitability of exoplanetary worlds. This is a highly debated subject as a number of models have been put forward, including the preservation of organic matter (OM) from the molecular cloud (Messenger, 2000), formation of OM in the relatively warm inner protoplanetary disk (Aléon, 2010) or during alteration on chondritic asteroids (Cody et al., 2011; Kebukawa et al., 2013; Cobb et al., 2015). Distinguishing between these various models requires better insights into the structure and chemical make-up of OM as well as the isotopic composition of light elements such as nitrogen, hydrogen and carbon. Importantly, spectral line observations of the isotopologues of N- and H-bearing species in star-forming regions allow us to track the formation of COMs from the molecular cloud to the protoplanetary disk stage. Various processes can lead to the synthesis of COMs, including ion–molecule reactions at low temperatures (<25 K) (Terzieva and Herbst, 2000; Rodgers and Charnley, 2008; Wirström et al., 2012; Hily-Blant et al., 2013a, 2013b) and photochemistry occurring in the molecular cloud (Clayton, 2002; Lyons, 2009; Heays et al., 2014) as well as Strecker synthesis on the parent body (Cody et al., 2011; Kebukawa et al., 2013; Cobb et al., 2015). These processes result in different degrees of N, H and C isotope fractionation (Terzieva and Herbst, 2000; Rodgers and Charnley, 2008; Wirström et al., 2012; Heays et al., 2014; Roueff et al., 2015), which will be reflected in the organic end-product. Hence, integrating the isotope composition and structure of OM may provide unique insights into the chemical and physical pathways leading to the formation of COMs. Recently, OM present in a number of primitive Solar System materials, including carbonaceous chondrites (CR, CM, CI, Tagish Lake), samples returned from comet 81P/Wild 2 and interplanetary dust particles (IDPs) have been investigated in this manner (Keller et al., 2004; Nakamura-Messenger et al., 2006; Busemann et al., 2006; Busemann et al., 2009; Zega et al., 2010; Cody et al., 2008; Cody et al., 2011; Vollmer et al., 2014; De Gregorio et al., 2010; De Gregorio et al., 2013; Le Guillou et al., 2014). COMs in meteorites can be divided into insoluble (IOM) and soluble (SOM) organic matter. IOM is more abundant in meteorites (70–99% of the total organics; Pizzarello et al., 2006) and consists of kerogen-like macromolecular carbon whereas SOM contains a complex suite of prebiotic molecules including carboxylic and amino acids (Pizzarello et al., 2006). The origins of IOM and SOM and their potential genetic relationship are still poorly understood. Some of these organics are thought to be very pristine and of interstellar origin based on their anomalous $^{15}N/^{14}N$ and D/H ratios. Nevertheless, the relative spatial and temporal formation regions of these primitive Solar System materials are not well constrained, which prevents a full understanding of the formation pathways of their OM.

Carbonaceous chondrites and comets show N and H isotope variations on a bulk scale, as well as for their OM and water reservoirs. For example, Oort Cloud comets (OCCs) record high ^{15}N and D enrichments for various molecular species (Bockelée-Morvan et al., 2015), whereas Jupiter Family comets (JFCs) show comparable ^{15}N excesses but variable D/H ratios that can be similar to the terrestrial composition (Hartogh et al., 2011; Altwegg et al., 2015). Chondritic lithic clasts from the Isheyevo CH/CB$_b$ meteorite, which are characterized by extreme ^{15}N-rich domains as well as high bulk ^{15}N enrichments, show D depletion relative to Earth (Bonal et al., 2010a). In contrast, CR chondrites that together with CH and CB chondrites belong to the metal-rich carbonaceous chondrites are typified by coupled ^{15}N and D enrichments (Busemann et al., 2006; Alexander et al., 2012). These observations suggest that differences in N and H isotope signals in various primitive bodies may be controlled by the accretion regions of their precursors, although the various chemical and physical processes that can modify the carriers of ^{15}N and D isotope anomalies during and after their incorporation into primitive bodies are poorly understood.

Chondrite lithic clasts from Isheyevo are characterized by small domains highly enriched in ^{15}N ($\delta^{15}N$ up to ~5000‰, where the δ notation represents the deviation

from the terrestrial reference value in ‰) (Briani et al., 2009; Bonal et al., 2010a). Together with other classes of metal-rich carbonaceous chondrites (i.e., CR, CB and CH), the parent body of the Isheyevo chondrite is believed to have accreted in a region distinct from most inner Solar System asteroidal bodies, possibly beyond the orbits of the gas giants (Van Kooten et al., 2016). It has been suggested that Isheyevo lithic clasts may have incorporated up to 50% of primordial molecular cloud material (Van Kooten et al., 2016) and, as such, these objects may preserve OM inherited from the protosolar molecular cloud core. Additionally, Isheyevo lithic clasts include lithologies aqueously altered to various degrees (Bonal et al., 2010a), which makes them excellent candidates to evaluate the effect of parent body processes on the isotopic composition and structure of OM. To better understand the origin of N and H isotope variability in the early Solar System, we have characterized the chemistry and petrology of multiple Isheyevo lithic clasts including the extensively hydrated (H-clasts) and weakly hydrated (A-clasts) and determined their N, H and C isotope compositions by secondary ion mass spectrometry (SIMS). Subsequently, ^{15}N-rich domains were extracted for transmission electron microscopy (TEM) analyses at sub-μm resolution to define the structure and composition of their OM. Additional clasts were selected for Mg and Cr isotope analyses by multi-collector inductively coupled plasma (MC-ICPMS) and thermal ionization mass spectrometry (TIMS), respectively. Our results reveal the existence of multiple, distinct organic precursors amongst the different clasts, which are characterized by variable levels of ^{15}N and D enrichment.

2. MATERIALS AND METHODS

2.1. Materials

Isheyevo is a CH/CB$_b$-chondrite that consists of two lithologies, comprising a dominant metal-rich one similar to CB$_b$ chondrites (50–90 vol% Fe,Ni metal) and a silicate-rich one that is similar to CH chondrites (7–50 vol % Fe,Ni metal) (Ivanova et al., 2008). Both lithologies contain metal, chondrules, refractory inclusions (CAIs and AOAs) and lithic clasts, although they show variations in modal abundances, chondrule size and proportions of porphyritic versus non-porphyritic chondrules (Ivanova et al., 2008). Like other metal-rich carbonaceous chondrites (CR, CH, CB), Isheyevo is characterized by large bulk ^{15}N enrichments (δ^{15}N > 1000‰). These enrichments have previously been attributed to ^{15}N carriers located in N_2-enriched impact-related vesicles, acid resistant residues and metal-sulfide complexes (Marty et al., 2010a). More recently, similar bulk enrichments were found in Isheyevo lithic clasts with ^{15}N-enriched domains up to 5000‰ (Briani et al., 2009; Bonal et al., 2010a). These regions were interpreted as OM formed in interstellar or outer Solar System cold environments where ion-molecule reactions take place.

Isheyevo lithic clasts can be divided into three main groups (Bonal et al., 2010b). In this work, we consider the two most abundant types, namely the extensively hydrated (H-clasts, ~60 vol%) and weakly hydrated clasts (A-clasts for *anhydrous*, ~30 vol%). H-clasts mostly consist of aqueous alteration products such as (framboidal) magnetite, sulfide laths, course phyllosilicates and dolomite grains embedded in a fine-grained matrix dominated by serpentine. The matrix of A-clasts is less hydrated and does not contain other hydration products besides phyllosilicates but instead contain anhydrous silicates such as Mg-rich olivines and pyroxenes. The A-clasts generally have higher bulk and localized ^{15}N-enrichments compared to the H-clasts. This discrepancy is attributed to ^{15}N dilution by aqueous alteration of the hydrated clasts or, alternatively, to different parent bodies and, hence, different N-bearing precursors for the clasts (Bonal et al., 2010a). Both lithic clast types are considered to represent one or more previously unsampled chondritic parent bodies and were incorporated into the Isheyevo host after/while it formed from an impact-vapor/melt plume (Krot et al., 2005), ~5 Myr after CAI formation (Krot et al., 2005; Bollard et al., 2015).

We selected five A-clasts and two H-clasts for N isotope measurements and three additional H-clasts for H isotope analyses. The carbonates from the H-clasts have previously been measured for ^{53}Mn-^{53}Cr isotope systematics (Van Kooten et al., 2016). In the same study, H-clasts were analyzed for their Mg and Cr isotope composition. Here, two additional H-clasts and three A-clasts have been selected for Mg- and Cr-isotope analyses. Finally, we have conducted a detailed investigation of ^{15}N-rich domains from both clast types using transmission electron microscopy (TEM) and NanoSIMS. All information relative to the material investigated and data collected is summarized in Table 1.

2.2. Electron microprobe

Back Scattered Electron (BSE) images of two Isheyevo slabs (10 × 5 cm) were made on a Scanning Electron Microscope (SEM, GEUS, Copenhagen) in order to identify lithic clasts. Only clasts larger than 500 μm were selected for the purpose of excavating them for Mg and Cr isotope measurements. Based on clast locations, 11 polished 1 inch diameter thick sections were cut for Electron Microprobe (EMP) analyses at the University of Hawai'i (UH). The sections were mapped on the UH Cameca SX-50 electron microprobe with a 1–2 μm/pixel resolution in Mg, Ca, Al, S and Ni Kα X-rays. The microprobe operated at 15 keV accelerating voltage, with a 50 nA beam current and 3 μm beam size. Additionally, high resolution BSE images were taken of the clasts selected for N and H isotope analyses, along with Ca, Mg, Fe, Al, S, Ni, Si, Na, P, Ti Kα X-ray maps (5 nA, 3 μm). Compositional EMP data for H-clasts have previously been reported in Van Kooten et al. (2016). This work will add the chemical composition of anhydrous silicates and matrices of A-clasts, which were measured on the EMP using a focused beam (5 nA, 5 μm).

2.3. Nitrogen and carbon isotope measurements

Nitrogen and carbon isotopes were measured on the UH Cameca ims-1280 ion microprobe (UH). Scanning isotope

Table 1
Overview of all analyses conducted on Isheyevo lithic clasts. H-clasts are designated 'H', while A-clasts are designated 'A'. N, C, H, Mg, Cr, O and Mn–Cr represent isotope analyses.

		Bulk						TEM	Carbonates	
Clasts		EMP	N	C	H	Mg	Cr		O	Mn-Cr
A1-1	A				x			x		
A3-2	H	x	x	x	x			x		x[†]
A5-4	H	x[†]	x	x	x					
B3-1	A	x	x	x	x	x	x			
B5-1	A	x	x	x	x					
B5-2	A	x	x	x	x					
B5–3	A	x	x	x	x			x		
A5-1	H	x[†]			x					
A1-3	A	x	x	x	x					
B1-3	H									x[†]
I4LC2	H		x[*]	x[*]					x[*]	x[†]
I4LC3	H								x[*]	x[†]
A4-1	H	x[†]								
A1–2	H	x								
A5-2	H	x [†]								
A5–3	H	x [†]								
A2-1	H					x[†]	x[†]			
A2-2	H					x[†]	x[†]			
A2-3	H					x[†]	x[†]			
B4-BC	H					x[†]	x[†]			
B4-1	H					x[†]	x[†]			
CdLC2	H					x	x			
CdLC3	H					x	x			
DLC4	A					x	x			
DLC6	A					x	x			

[*] Analyses carried out by Bonal et al. (2010a).
[†] Analyses carried out by Van Kooten et al. (2016).

images were taken of five A-clasts and two H-clasts, for $^{12}C^{14}N^-$, $^{12}C^{15}N^-$, $^{18}O^-$, $^{28}Si^-$, $^{12}C^-$, $^{13}C^-$ and H^- with a 10 pA Cs^+ primary ion beam. We note that $^{12}C^{14}N^-$ and $^{12}C^{15}N^-$ ions can be derived from organically bound N, but also from 'free N' that recombines with secondary C-ions. All secondary ions were measured on a monocollector EM with a mass-resolving power (MRP) of 6500, except for H^-, which was collected on a multicollector EM, with a MRP of 2000. $^{12}C^-$, $^{18}O^-$, $^{12}C^{14}N^-$ and $^{28}Si^-$ were measured for 1s, H^- for 2 s, while $^{13}C^-$ and $^{12}C^{15}N^-$ were measured for 30 s per cycle. Each measurement ran for 80 cycles and a mass calibration was performed between pre-sputtering and the measurement. Pre-sputtering was done to remove the carbon coating on the sample in a 60 × 60 μm raster, for 300 s with a 5 nA ion beam. Raster images of 50 × 50 μm were made on 2–4 locations per clast, to get a representative average of the bulk isotopic composition. These locations were selected in the matrix, because the ^{15}N carrier is believed to reside in the insoluble organic material (IOM) embedded in the phyllosilicates (Bonal et al., 2010a; Alexander et al., 2007). To correct for instrumental mass fractionation (IMF), the Orgueil CI chondrite was used as a reference standard and measured between and after analysis of unknowns. The $\delta^{15}N$ ($\delta^{15}N_{av}$ = 46‰) and $\delta^{13}C$ ($\delta^{13}C_{av}$ = −14‰) values of this standard are well documented (Alexander et al., 2007; Injerd and Kaplan, 1974; Robert and Epstein, 1982; Kerridge, 1985) and Orgueil resembles the clast matrices in texture and composition. L'image software (L. Nittler, DTM, Carnegie Inst. Washington) was used to process the SIMS images, to correct for raster shift and deadtime during measurements. Data interpolation for temporal shift in monocollector mode was done using formulas from Coakley et al. (2005). Bulk $\delta^{15}N$ values were derived by calculating the $^{12}C^{15}N^-$ over $^{12}C^{14}N^-$ ratio of the sum of 40 cycles after all corrections, dividing these measured values (*meas*) by the $^{15}N/^{14}N$ ratio for air ($^{15}N/^{14}N_{air} = 0.003676$) and converting them to delta notation:

$$\delta^{15}N\ (‰) = \left(\frac{^{15}N/^{14}N_{meas}}{^{15}N/^{14}N_{air}} - 1\right) \times 1000 \quad (1)$$

The standard error of the mean was propagated after IMF corrections according to Fitzsimons et al. (2000). Only the last 40 cycles typically characterized by stable count rates were used.

2.4. Hydrogen isotope measurements

Care was taken with Isheyevo thick sections to expose them to a minimal amount of terrestrial water before measuring H isotopes on the ion microprobe. Two weeks prior to measurements, samples were stored in a vacuum oven at 50 °C, to remove any adsorbed water. Samples were then moved quickly to sample chamber of the SIMS (UH) and

left there ~4 h until vacuum was restored. A liquid nitrogen cold trap equipped to the sample chamber was used during measurements. Pre-sputtering was set to 480 s in a 25 × 25 μm raster. The beam size was 10–15 μm, due to the high beam current (4 nA) that was necessary to prevent any hydrogen moving back to the center of the raster area. To avoid hydrogen contamination from the surrounding area, a sample raster of 15 × 15 μm was made with the same settings as pre-sputter mode and the e-gate was set to 50%, to sample the innermost area of the sample raster. H isotopes were measured with an O^- primary beam near locations of N isotope measurements in the matrix. By using an O^- primary beam, we ensured that we predominantly measured the isotopic composition of water bound in phyllosilicates with negligible contamination from organic material (Deloule and Robert, 1995; Bonal et al., 2010a; Piani et al., 2012). This is a result of the ionization efficiency as well as the abundance of hydrogen in phyllosilicates being at least an order of magnitude higher than in organics. Since the phyllosilicate compositions of lithic clasts in Isheyevo closely resemble serpentines (Bonal et al., 2010b), two endmembers of the serpentine group (antigorite: $[Mg, Fe^{2+}]_3Si_2O_5[OH]_4$ and chrysotile: $Mg_3SiO_5[OH]_4$) were chosen as standards to be measured in between sample runs to correct for IMF (Alt and Shanks, 2006). The fractionation factors observed for antigorite ($\alpha = 0.76$) and chrysotile ($\alpha = 0.74$) are very similar and result in shifts of ~30‰ when correcting our samples for IMF, within the typical uncertainty of our measurements. Applying this IMF correction to our Orgueil reference standard results in $\delta D = -127 \pm 29‰$, similar to the calculated phyllosilicate composition of Orgueil (Alexander et al., 2010). During each run, which consisted of 40 cycles (~60 s per cycle), we measured $^1H^+$ (1 s), D^+ (40 s), $^{24}Mg^{2+}$ (1 s), $^{12}C^+$ (1 s), $^{44}Ca^{2+}$ (1 s) and $^{30}Si^+$ (1 s) in mono-collector mode with a MRP of ~2100. Five standard runs were done with a hydrogen background check before and after the run. Average background counts were 20 cps for hydrogen, while during an average standard or sample run 10^5 cps were measured. Dead time, time interpolation and IMF corrections were similar to those done on nitrogen and carbon isotopes. Hydrogen isotope data is presented in the delta notation, which is the D/H (deuterium/hydrogen) ratio of the measured sample (*meas*) over the standard mean ocean water (*SMOW*):

$$\delta D(‰) = \left(\frac{D/H_{meas}}{D/H_{SMOW}} - 1\right) \times 1000 \quad (2)$$

2.5. Transmission Electron Microscopy (TEM) and NanoSIMS

Three lithic clasts targeted for N and H bulk isotope measurements were used for further analysis of ^{15}N-rich domains by TEM. Detailed BSE images of areas measured for N isotopes were taken by SEM and compared to $^{28}Si^-$, $^{12}C^-$ and $^{12}C^{15}N^-/^{12}C^{14}N^-$ raster images to find ^{15}N-rich domains. These regions were then carefully extracted by focused ion beam (FIB) in situ lift-out technique with an FEI Helios SEM, equipped with an EDAX SD Apollo 10 Pegasus EDS and an Omniprobe manipulator (DTU-Cen, Denmark). Before the lift-out, the ^{15}N-rich domain was covered by a platinum organometallic complex ($C_9H_{16}Pt$) of 2 (h) × 2 (w) × 20 (l) μm to protect the sample from unwanted damage due to a Ga ion beam, using first an electron beam and subsequently a Ga^+ beam to make a denser PtC protection layer. The section was then freed by stepwise ion-milling and attached to a Cu TEM half-grid, where it was thinned to electron transparency (~100 nm) using a 30 kV Ga ion beam at currents reduced from 3 nA to 10 pA as the sample became thinner and a 2 kV Ga ion beam for final polishing. During the FIB lift-out procedure the preparation advancement of the thin sections was occasionally observed using an electron beam with an estimated total dose of 10^3-10^4 e/nm^2. We note that the dose amount during the FIB preparation was much lower than the amount used in the EELS measurements (typically 2–5 × 10^7 e/nm^2). The samples were then transported to an FEI Titan 80-300ST TEM, where Bright Field (BF) and High-Angle Annular Dark Field (HAADF) images were taken in STEM mode. Subsequently, Electron Energy-Loss Spectra (EELS) were done in TEM diffraction mode, operating at 120 kV and using a beam diameter of 100 nm with acquisition times of 200 s. Using the TEM mode reduced significantly self-contamination of the sample during electron irradiation. A monochromator was used to obtain a high energy resolution of 0.1–0.2 eV, which provided distinct peak separations in carbon-K and nitrogen-K edges. Background subtracted spectra were normalized to the total carbon at 320 eV. To calculate the C/N ratios, we used the following equation from Lajaunie et al. (2015):

$$\frac{N_C}{N_N} = \frac{I_C}{I_N} \times \frac{\sigma_N}{\sigma_C}, \quad (3)$$

where the σ is the partial ionization cross section (calculated with Sigmak software in Fortran, with an energy window of 35 eV, a 120 keV incident beam and a 100 mrad collection angle) and I_C is the integral of the total carbon with an energy window of 285–320 eV and I_N is the integral of the total nitrogen with an energy window of 400–435 eV.

The three thin sections used for TEM analyses were transported to the Open University (Milton Keynes, UK) for investigation of the ^{15}N carrier. The samples attached to their copper TEM grids were gold coated on both sides (20 nm thickness) and subsequently deposited on double-sided sticky carbon pads. This procedure was necessary to achieve good charge compensation/dissipation in order to achieve the necessary count rates and MRP (>8000). Samples were pre-sputtered gently with a ~10 pA primary Cs^+ beam for ~30 min until sputter equilibrium was achieved. For analyses, a beam current of 0.67 pA was used, providing a spatial resolution of ~100 nm. The primary beam was rastered over 5 × 5 μm (128 × 128 pixels) for 8.2 s per plane, and we collected up to 300 planes on each area. The secondary ions of $^{16}O^-$, $^{12}C_2^-$, $^{12}C^{14}N^-$, $^{12}C^{15}N^-$ and $^{28}Si^-$ were measured in multi-collection mode. Before and after sample analyses, a sample of hydroxybenzotriazole standard was measured using the same settings to make IMF corrections. The results were processed using L'image software, including correction for detector deadtime (44 ns) and sample drift.

2.6. Magnesium and chromium isotope measurements

Five H-clasts have been measured previously for Mg and Cr isotopes (Van Kooten et al., 2016), but have not been measured for N and H isotopes. In addition to these clasts, we sampled another five clasts for Mg and Cr isotope analyses. Three of these clasts have been classified as A-clasts and one out of three has been measured for N and H isotope data. The other two clasts are H-clasts. The sampling, digesting and chemical purification of all samples was done as in Van Kooten et al. (2016). The isotopic composition of the purified Mg was determined using the Neptune Plus MC-ICPMS at the Natural History Museum of Denmark and full analytical procedures are reported in Bizzarro et al. (2011). Samples were aspirated into the plasma source by means of an Apex sample introduction system with an uptake rate of ~16 μL/min, and the Mg isotope composition was measured in high-resolution mode ($M/\Delta M > 5000$). Using this approach, the sensitivity of the instrument was ~50 V ppm^{-1} and samples were typically analyzed with a signal intensity of 30 V on mass ^{24}Mg. Single analyses comprised 1410 s of data acquisition followed by 570 s of baseline measurements obtained on-peak. Each sample was bracketed by standard analyses and systematically analyzed ten times. Mg isotope data are reported in the μ-notation as relative deviations from the DTS-2b standard according to the following formula:

$$\mu^{x}Mg(ppm) = \left(\frac{{}^{x}Mg/{}^{24}Mg_{meas}}{{}^{x}Mg/{}^{24}Mg_{DTS-2b}} - 1\right) \times 10^{6}, \quad (4)$$

where x represent mass 25 or 26. The mass-independent component in ^{26}Mg ($\mu^{26}Mg^{*}$) is reported in the same fashion, but represents deviations from the internally normalized ^{26}Mg/^{24}Mg of the sample from the reference standard, normalized to ^{25}Mg/^{24}Mg = 0.126896 (Bizzarro et al., 2011) using the exponential mass fractionation law ($\beta = 0.511$). All Mg data reduction was conducted off-line using the freely distributed Iolite data reduction package which runs within Igor Pro (Paton et al., 2011) and changes in mass bias with time were interpolated using a smoothed cubic spline. For each analysis, the mean and standard error of the measured ratios were calculated using a 3 SD threshold to reject outliers. Individual analyses of a sample were combined to produce an average weighted by the propagated uncertainties of individual analyses and reported final uncertainties are the 2SE of the mean. The external reproducibility of our measurements using this method is 20 and 2.5 ppm for the μ^{25}Mg and $\mu^{26}Mg^{*}$, respectively. The ^{27}Al/^{24}Mg ratios were measured on an X-series ICPMS at the Centre for Star and Planet Formation and are accurate to 2%. The isotopic composition of the purified Cr was determined using the Triton TIMS at the Natural History Museum of Denmark using a sample standard bracketing approach described in Van Kooten et al. (2016). During each analysis, ^{51}V, ^{56}Fe and ^{49}Ti were collected together with the Cr-isotopes of interest (^{50}Cr, ^{52}Cr, ^{53}Cr and ^{54}Cr) to check for interferences of ^{50}V, ^{54}Fe and ^{50}Ti. We never observed any significant ^{49}Ti or ^{51}V, whereas ^{56}Fe was typically <10 mV. Each sample measurement consists of the average and standard error of at least five individual ~20 ng filament loads, calculated using a 2 SD outlier rejection scheme. Sample analyses were interspaced with analyses of ~20 ng filament loads of the SRM-3112a standard, measured under the same conditions as the samples. Individual analyses typically consist of 500 s to 1500 s of data acquisitions, with typical internal precision of 20 ppm for the ^{54}Cr/^{52}Cr ratio. Electronic baselines were measured at the beginning and end of individual sessions. The ^{54}Cr/^{52}Cr data are reported in the μ notation according to the following formula:

$$\mu^{x}Cr(ppm) = \left(\frac{{}^{x}Cr/{}^{52}Cr_{meas}}{{}^{x}Cr/{}^{52}Cr_{SRM-3112a}} - 1\right) \times 10^{6}, \quad (5)$$

where the ^{x}Cr/^{52}Cr values reflect the internally normalized values, normalized to ^{52}Cr/^{50}Cr = 19.2832 Van Kooten et al., 2016 using the exponential mass fractionation law. The uncertainties of the ^{54}Cr/^{52}Cr measurements quoted in Table 3 reflect the internal precision of the measurement. The external reproducibility of our measurements using this method is 12 ppm for the μ^{54}Cr.

3. RESULTS

3.1. Mineral chemistry of Isheyevo lithic clasts

Isheyevo lithic clast mineral compositions are presented in Table 2 and Fig. 1. H-clasts mainly consist of hydrated matrix composed of phyllosilicates, dolomite, (framboidal) magnetite and iron sulfides. Their phyllosilicates, both coarse- and fine-grained, are dominantly serpentines that compositionally overlap with CR, CM and CI chondrite matrices (Fig. 1). Secondary alteration products such as sulfides, magnetite and carbonates are absent in A-clasts, but large phyllosilicates, although rare, are present with compositions indistinguishable from H-clasts (Fig. 1). The phyllosilicate compositions for H- and A-clasts are in agreement with results from Bonal et al. (2010a), but span a larger compositional range. Based on total major element weight percentages of the fine-grained matrix, we infer that A-clast matrix has a lower water content than H-clasts (up to 10 wt% less) and higher abundances of sulfur (up to 7 wt %). A-clasts additionally contain abundant anhydrous silicates and FeNi metal beads that are embedded in the matrix and are up to ~100 μm in size. Most of these silicates are Mg-rich low-Ca pyroxenes (En_{97-99}), whereas olivines are less abundant and compositionally more variable (Fo_{83-98}, Table 2). Lastly, A-clasts can contain porphyritic and cryptocrystalline chondrules or chondrule fragments similar to chondrules from CH and CB chondrites. Overall, A-clasts appear to have experienced a lesser amount of parent body alteration than H-clasts.

3.2. N, H and C isotope composition of Isheyevo lithic clasts

3.2.1. N and C isotope compositions obtained by SIMS

Nitrogen and carbon isotope measurements were carried out on matrix regions of the lithic clasts (Electronic Annex, Figs. S1 and S2) and are presented in Table 3. For these regions, we find ranges of bulk δ^{15}N compositions from 57 ± 23 to 178 ± 24‰ for H-clasts and from 186 ± 24 to

Table 2
Representative average compositions of minerals and matrices from six A-clasts (in wt%). *n* = number of individual analyses, px = pyroxene, ol = olivine, ph = phyllosilicate, fm = fine-grained matrix, plg = plagioclase, cm = coarse-grained matrix. Errors are presented in brackets and are 2SD, except for single analyses that are awarded an internal error of 0.1 wt%.

		n	SiO_2	TiO_2	Al_2O_3	FeO	MnO	MgO	CaO	Na_2O	SO_3	Cr_2O_3	Total
B5-2	px	8	54.5 (3.9)	0.3 (0.3)	3.4 (3.4)	2.3 (1.8)	0.3 (0.2)	33.7 (8.5)	5.6 (7.9)	0.0 (0.0)	0.1 (0.1)	0.6 (0.4)	100.8
	ol	2	40.4 (2.6)	0.0 (0.0)	0.0 (0.0)	12.3 (12.9)	0.2 (0.2)	47.2 (11.3)	0.1 (0.1)	0.0 (0.0)	0.0 (0.0)	0.3 (0.1)	100.7
	ph	1	30.6 (0.1)	0.0 (0.1)	0.0 (0.1)	23.5 (0.1)	0.0 (0.1)	39.5 (0.1)	0.3 (0.1)	0.0 (0.1)	0.3 (0.1)	0.7 (0.1)	95.0
	fm	2	31.0 (2.0)	0.1 (0.1)	1.9 (0.1)	28.3 (1.8)	0.2 (0.1)	16.8 (1.4)	1.1 (0.1)	0.1 (0.0)	7.1 (2.0)	0.4 (0.0)	87.0
B5-1	px	6	54.0 (2.2)	0.2 (0.2)	2.2 (1.8)	1.7 (1.2)	0.1 (0.1)	38.5 (6.4)	3.5 (4.4)	0.0 (0.0)	0.1 (0.0)	0.6 (0.2)	100.8
	ph	3	24.4 (12.3)	0.0 (0.0)	1.0 (0.7)	44.7 (12.6)	0.2 (0.1)	10.7 (8.3)	0.5 (0.2)	0.1 (0.1)	1.3 (0.9)	0.4 (0.3)	83.3
	fm	2	31.5 (3.7)	0.1 (0.0)	1.7 (0.2)	27.1 (3.6)	0.2 (0.0)	17.8 (2.0)	1.1 (0.1)	0.1 (0.0)	6.7 (3.1)	0.4 (0.1)	86.6
B5–3	ch	2	56.5 (0.9)	0.0 (0.0)	0.0 (0.0)	4.7 (0.6)	0.1 (0.1)	36.0 (0.7)	0.1 (0.0)	0.0 (0.0)	0.1 (0.0)	0.7 (0.1)	98.2
	px	2	50.0 (3.5)	0.1 (0.0)	2.2 (1.3)	1.9 (2.2)	0.1 (0.0)	43.4 (5.4)	1.8 (0.8)	0.0 (0.0)	0.0 (0.1)	0.6 (0.1)	100.2
	ch	2	41.6 (0.0)	0.0 (0.0)	0.1 (0.0)	2.0 (0.1)	0.1 (0.0)	55.1 (0.3)	0.2 (0.0)	0.0 (0.0)	0.0 (0.0)	0.6 (0.1)	99.6
	fm	5	31.7 (2.3)	0.1 (0.0)	2.0 (0.2)	24.9 (5.9)	0.2 (0.1)	21.6 (8.6)	1.3 (0.7)	0.1 (0.1)	6.4 (3.3)	0.5 (0.3)	88.8
A1–2	px	6	58.8 (2.0)	0.0 (0.0)	0.2 (0.2)	1.6 (2.0)	0.0 (0.0)	39.3 (2.1)	0.2 (0.1)	0.0 (0.0)	0.0 (0.0)	0.0 (0.0)	100.3
	plg	2	65.2 (2.5)	0.0 (0.0)	19.0 (0.3)	1.1 (0.7)	0.0 (0.0)	0.9 (0.8)	0.9 (0.2)	9.4 (1.1)	0.0 (0.0)	0.0 (0.0)	96.6
	ol	1	39.7 (0.1)	0.1 (0.1)	0.0 (0.1)	15.6 (0.1)	0.2 (0.1)	44.0 (0.1)	0.1 (0.1)	0.0 (0.1)	0.1 (0.1)	0.2 (0.1)	99.9
	cm	2	51.1 (3.0)	0.1 (0.0)	4.3 (1.9)	18.5 (1.2)	0.6 (0.1)	14.8 (2.9)	2.9 (0.2)	0.9 (0.1)	0.2 (0.2)	0.6 (0.3)	94.0
A1-3	px	4	51.0 (2.0)	0.2 (0.2)	4.9 (3.4)	0.9 (0.1)	0.0 (0.0)	38.5 (7.8)	4.7 (5.1)	0.0 (0.0)	0.0 (0.0)	0.6 (0.2)	100.9
	ol	1	42.9 (0.1)	0.1 (0.1)	0.1 (0.1)	1.8 (0.1)	0.0 (0.1)	57.4 (0.1)	0.2 (0.1)	0.0 (0.1)	0.0 (0.1)	0.5 (0.1)	103.2
	ph	3	34.6 (6.1)	0.2 (0.3)	4.5 (7.3)	14.1 (10.5)	0.2 (0.1)	34.7 (11.0)	3.5 (5.4)	0.1 (0.1)	0.6 (0.1)	0.7 (0.0)	93.0
	fm	3	32.0 (1.0)	0.1 (0.0)	2.0 (0.5)	27.2 (1.0)	0.3 (0.0)	19.6 (2.5)	0.9 (0.4)	0.3 (0.1)	7.7 (2.3)	0.5 (0.1)	90.5
B3-1	px	2	54.9 (4.2)	0.1 (0.1)	1.2 (1.6)	1.0 (0.4)	0.1 (0.1)	40.8 (0.9)	1.2 (1.1)	0.1 (0.1)	0.0 (0.0)	0.4 (0.5)	99.8
	ol	1	40.1 (0.1)	0.0 (0.1)	0.4 (0.1)	4.9 (0.1)	0.3 (0.1)	52.9 (0.1)	0.1 (0.1)	0.0 (0.1)	0.1 (0.1)	0.6 (0.1)	99.4
	fm	5	30.5 (2.9)	0.1 (0.0)	1.6 (0.6)	28.7 (5.4)	0.2 (0.1)	20.6 (7.6)	0.7 (0.3)	0.1 (0.1)	6.2 (2.3)	0.5 (0.2)	89.3

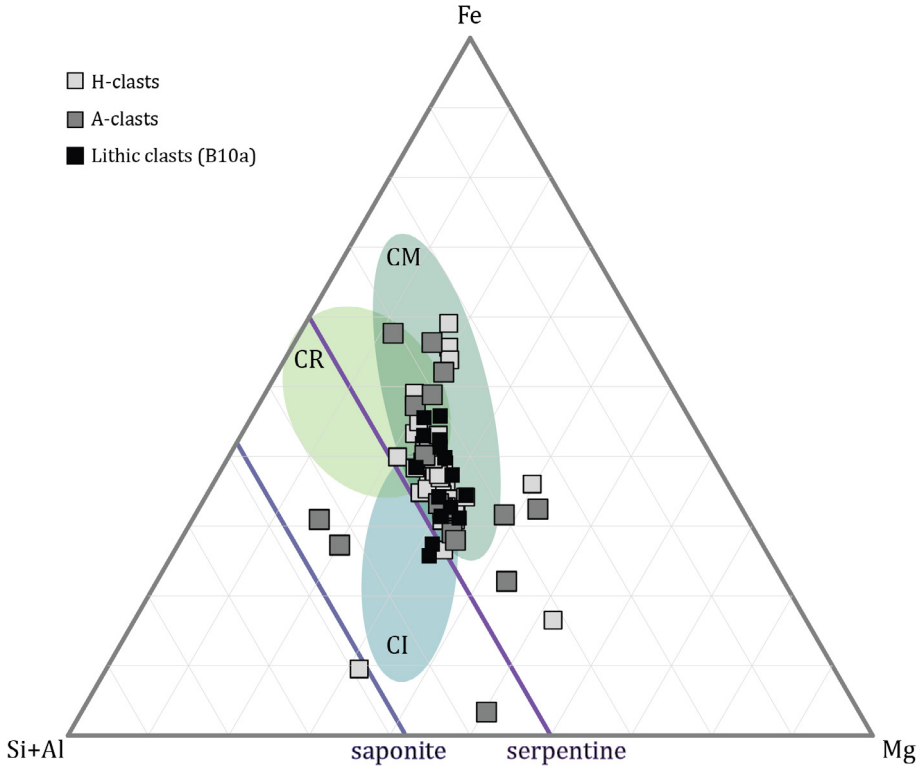

Fig. 1. Phyllosilicate compositions of lithic clasts in ternary diagram with endmember compositions of relative abundances of Fe, Mg and Si + Al, calculated from their weight percentages. Black squares represent lithic clasts from Bonal et al. (2010b) and grey squares are A- and H-clasts from this work and Van Kooten et al. (2016), respectively. Green shaded fields represent compositional ranges from CR, CI and CM chondrites using data from Weisberg et al. (1993), Bunch and Chang (1980), Tomeoka and Buseck (1988). Also given are solid solution lines for serpentine and saponite.

643 ± 32‰ for A-clasts, with ^{15}N-rich domains up to 432 ± 39‰ and 5169 ± 454‰, respectively. Carbon isotope data for the same matrix regions have δ^{13}C values between 0‰ and −20‰ and are indistinguishable from other chondrite groups (Grady and Wright, 2003). Previous N isotope analyses on two Isheyevo lithic clasts generally show higher and more narrow range of δ^{15}N values for both H-clasts and A-clasts (Table 3, Bonal et al., 2010a). To compare N isotope datasets, it is necessary to eliminate the possibility of a systematic offset caused by differences in instrumental setup or data processing. Nitrogen isotope data from Bonal et al. (2010a) and this work were both measured on the UH Cameca ims-1280 ion microprobe. Setup conditions were similar, the largest difference being the total run time (600 cycles in Bonal et al., 2010a). The use of a shorter run time (80 cycles, this work) may affect the outcome if there is an inconsistent time dependent variation between $^{12}C^{14}N^-$ and $^{12}C^{15}N^-$ counts. However, while the count rate slowly decreased over time, the ratio of $^{12}C^{15}N^-$ over $^{12}C^{14}N^-$ (cps) remained constant throughout runs. Nevertheless, only the last 40 cycles of each run were taken into account, as the count rate was most stable during this interval. The most important effect on the N isotope data results from the data processing with L'image software, using image aligning and smoothing tools as well as selection of regions of interest. ^{15}N-rich isotope domains are most affected by this process, but the bulk isotope data will only change by a few tens of permill. Hence, the difference of >400‰ between A-clasts measured in this work and in Bonal et al. (2010a) cannot be explained by differences in data reduction. Additionally, the range of ^{15}N-rich domains from both datasets is similar and overlaps with each other. Hence, we can rule out data reduction processes as a cause for variations in N isotope data sets. Collectively, our data show that A-clasts have a wider N isotope range than previously observed (Bonal et al., 2010a), varying from bulk δ^{15}N values comparable to CR chondrites (<200‰, Fig. 2a) to bulk values that are higher than comets (>800‰, Fig. 2a). In contrast, H-clasts have a relatively narrow range of N isotope compositions that are typically similar or lower than CR chondrites.

3.2.2. H isotope compositions obtained by SIMS

Hydrogen isotope analyses were carried out on matrix regions close to N isotope rasters. Our data show overlapping but significantly distinct ranges, with H-clasts typically being more enriched in D (δD = +4 ± 71‰ to −217 ± 57‰) than A-clasts (δD = −144 ± 161‰ to −296 ± 65‰). Both clast types have D/H values between protosolar and terrestrial (Fig. 2b). In contrast to the N isotope data, the H isotope data for the lithic clasts are more comparable to CI/CM-type carbonaceous chondrites. Depletions in deuterium for Isheyevo lithic clasts relative to the terrestrial value (δD = 0‰) are in agreement with data

Table 3
Nitrogen, carbon and hydrogen isotope data of bulk lithic clasts (B) and their ^{15}N-rich domains (hs, for hotspots) for Orgueil, H-clasts and A-clasts. Errors are presented in 2SE. H_2O contents are calculated based on the Si/H ratio and H_2O content of our chrysotile standard and compared to literature (Alt and Shanks, 2006).

		$\delta^{15}N$ (‰)	$^{14}N/^{15}N$	$\delta^{13}C$ (‰)	δD (‰)	D/H	Si/H	H_2O (wt%)
Orgueil (CI) (1)	B	77 ± 21	253	−26 ± 26	−131 ± 55	1.35E−04	23	7.94
Orgueil (CI) (2)	B	39 ± 21	262	−41 ± 26	−118 ± 47	1.37E−04	24	7.63
Orgueil (CI) (3)	B	31 ± 20	264	−14 ± 21	−148 ± 95	1.33E−04	24	7.55
Orgueil (CI) (4)	B	46 ± 20	260	−8 ± 21	−128 ± 66	1.36E−04	24	7.68
H-clasts								
A3-2 (1)*	B	103 ± 22	247	18 ± 22	−58 ± 73	1.47E−04	18	10.34
A3-2 (2)	B	178 ± 24	231	3 ± 22	−92 ± 64	1.41E−04	16	11.18
A3-2 (3)	B	164 ± 23	234	−9 ± 22				
A5-4 (1)	B	57 ± 23	257	−20 ± 25	−217 ± 57	1.22E−04	11	15.81
A5-4 (2)	B	160 ± 23	235	−20 ± 25	−160 ± 25	1.31E−04	14	12.79
A5-4 (2)	hs	432 ± 39	190	−30 ± 25				
A1-1 (1)	B				−25 ± 59	1.52E−04	20	9.32
A1-1 (2)	B				4 ± 71	1.56E−04	20	8.95
A3-3 (1)	B				−6 ± 69	1.55E−04	16	11.28
A3-3 (2)	B				−51 ± 77	1.48E−04	17	10.56
A5c-1 (1)	B				−133 ± 46	1.35E−04	18	9.98
A5c-1 (2)	B				−76 ± 54	1.44E−04	19	9.81
4-LC2 (1)‡	B	154 ± 55	236	−4 ± 38				
I4-LC2 (2)‡	B	216 ± 83	224	6 ± 15				
I4-LC12 (1)‡	B	218 ± 49	223	14 ± 21				
I4-LC12 (2)‡	B	234 ± 52	220	3 ± 30				
I4-LC13 (1)‡	B	304 ± 120	209	−13 ± 29				
I4-LC13 (2)‡	B	381 ± 43	197	−14 ± 21				
UHC-1‡	B				−124	1.36E−04		
UHC-2‡	B				−65	1.46E−04		
A-clasts								
A1-3 (2)	B	301 ± 27	209	−14 ± 21	−296 ± 65	1.10E−04	30	6.10
A1-3 (3)	B	344 ± 27	202	−19 ± 21	−248 ± 22	1.17E−04	35	5.19
A1-3 (2)	hs	1776 ± 227	98	−14 ± 21				
A1-3 (2)	hs	1173 ± 86	125	−14 ± 21				
A1-3 (2)	hs	1010 ± 99	135	−14 ± 21				
A1-3 (3)*	hs	3534 ± 123	60	−19 ± 21				
B3-1 (1)†	B	186 ± 24	229	−13 ± 23	−229 ± 69	1.20E−04	37	4.97
B3-1 (2)†	B	236 ± 27	220	−11 ± 26	−216 ± 69	1.22E−04	39	4.68
B3-1 (1)	hs	1067 ± 75	132	−13 ± 23				
B3-1 (1)	hs	1308 ± 102	118	−13 ± 23				
B3-1 (2)	hs	656 ± 60	164	−11 ± 26				
B3-1 (2)	hs	1139 ± 164	127	−11 ± 26				
B5-1 (1)	B	590 ± 31	171	−19 ± 20	−216 ± 121	1.22E−04	59	3.08
B5-1 (2)	B	618 ± 32	168	−13 ± 20	−204 ± 77	1.24E−04	53	3.46
B5-1 (3)	B	611 ± 32	169	−7 ± 20				
B5-1 (4)	B	591 ± 31	171	−21 ± 20				
B5-1 (1)	hs	2200 ± 90	85	−19 ± 20				
B5-1 (1)	hs	2497 ± 150	78	−19 ± 20				
B5-1 (2)	hs	2554 ± 149	77	−13 ± 20				
B5-1 (3)	hs	2920 ± 166	69	−7 ± 20				
B5-1 (4)	hs	3825 ± 263	56	−21 ± 20				
B5-2 (1)	B	643 ± 32	166	−11 ± 21	−229 ± 64	1.20E−04	46	3.96
B5-2 (2)	B	569 ± 32	173	−22 ± 21	−252 ± 79	1.17E−04	36	5.11
B5-2 (1)	hs	4219 ± 285	52	−11 ± 21				
B5-2 (1)	hs	4800 ± 411	47	−11 ± 21				
B5-2 (2)	hs	3667 ± 175	58	−22 ± 21				
B5-2 (2)	hs	5169 ± 454	44	−22 ± 21				

(*continued on next page*)

Table 3 (*continued*)

		$\delta^{15}N$ (‰)	$^{14}N/^{15}N$	$\delta^{13}C$ (‰)	δD (‰)	D/H	Si/H	H_2O (wt%)
B5–3 (1)	B	606 ± 33	169	−12 ± 22	−144 ± 161	1.33E−04	51	3.56
B5–3 (2)	B	635 ± 34	166	2 ± 21	−251 ± 65	1.17E−04	37	4.93
B5–3 (1)*	hs	2186 ± 119	85	−12 ± 22				
B5–3 (2)	hs	3853 ± 280	56	2 ± 21				
I7-LC22 (1)‡	B	1166 ± 55	126	−5 ± 20				
I7-LC22 (2)‡	B	1250 ± 54	121	−2 ± 11				
I7-LC23 (1)‡	B	1093 ± 70	130	−16 ± 27				
I7-LC23 (2)‡	B	1245 ± 25	121	−9 ± 33				
I8-LC100B	B				−315	1.07E−04		
I8-LC101B	B				−245	1.18E−04		

† Clasts extracted for Mg and Cr-isotope analyses.
‡ Data from Bonal et al. (2010a).
* ^{15}N-rich domains extracted for TEM analyses.

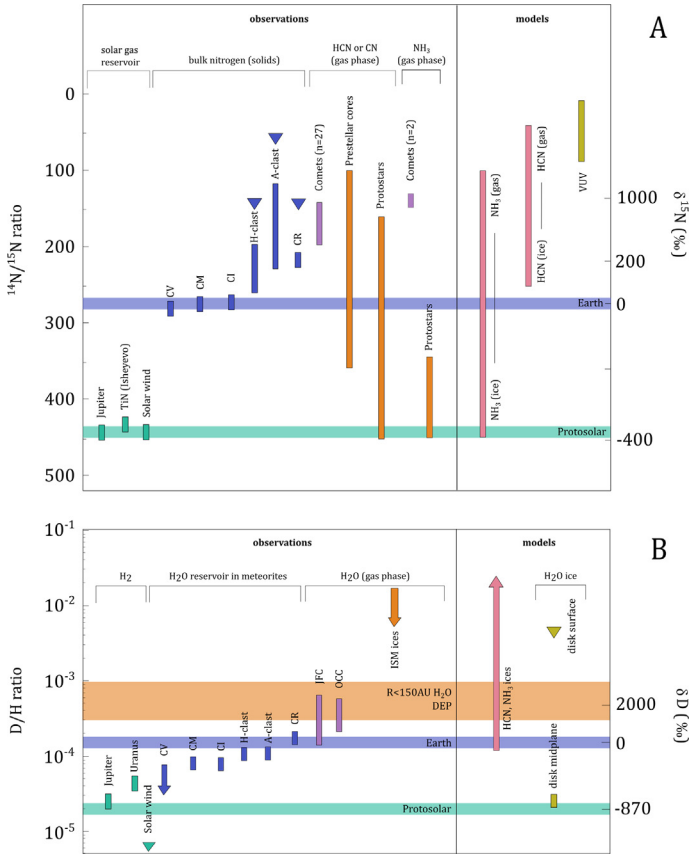

Fig. 2. Summary plots for N (panel A) and H (panel B) isotope data. Data is given in ratios (left *y*-axes) as well as in delta notation (right *y*-axes), where δD is given against standard mean ocean water and $\delta^{15}N$ against terrestrial atmosphere. Nitrogen isotope data is compiled for Jupiter, TiN (Isheyevo) solar wind, prestellar cores and protostars (Wampfler et al., 2014), cometary data (Bockelée-Morvan et al., 2015), Isheyevo lithic clasts (this work), CV, CM, CI and CR chondrites (Alexander et al., 2007), modeled HCN and NH_3 ices (Wirström et al., 2012) and modeled enrichments in N_2 by VUV irradiation on the disk surface (Chakraborty et al., 2014). The triangles represent enriched domains. Hydrogen isotope plot is modified from Cleeves et al. (2014) (their Fig. 1), with additional data for an upper limit H isotope composition Solar Wind (Huss et al., 2012), Isheyevo lithic clasts (this work), CV and CR chondrites (Alexander et al., 2012), Jupiter Family Comets (JFC) (Bockelée-Morvan et al., 2015), modeled D/H ratios for HCN and NH_3 ices (Wirström et al., 2012) and modeled D/H in a protoplanetary disk for the midplane ($Z < 40$ AU) and for a negligibly thin surface layer (Cleeves et al., 2016). DEP = deeply embedded protostars.

from Bonal et al. (2010a), who found δD values of −245 and −315‰ for two A-clasts and −124 and −65‰ for two H-clasts (Table 3). Briani et al. (2009) on the other hand, found δD values ranging from −70 to +420‰ for four lithic clasts (no group assigned) and PX-18 (assigned group IV), which is significantly higher than our data. However, Briani et al. (2009) measured H isotopes using a Cs^+ beam and kerogen as a standard. A Cs^+ primary

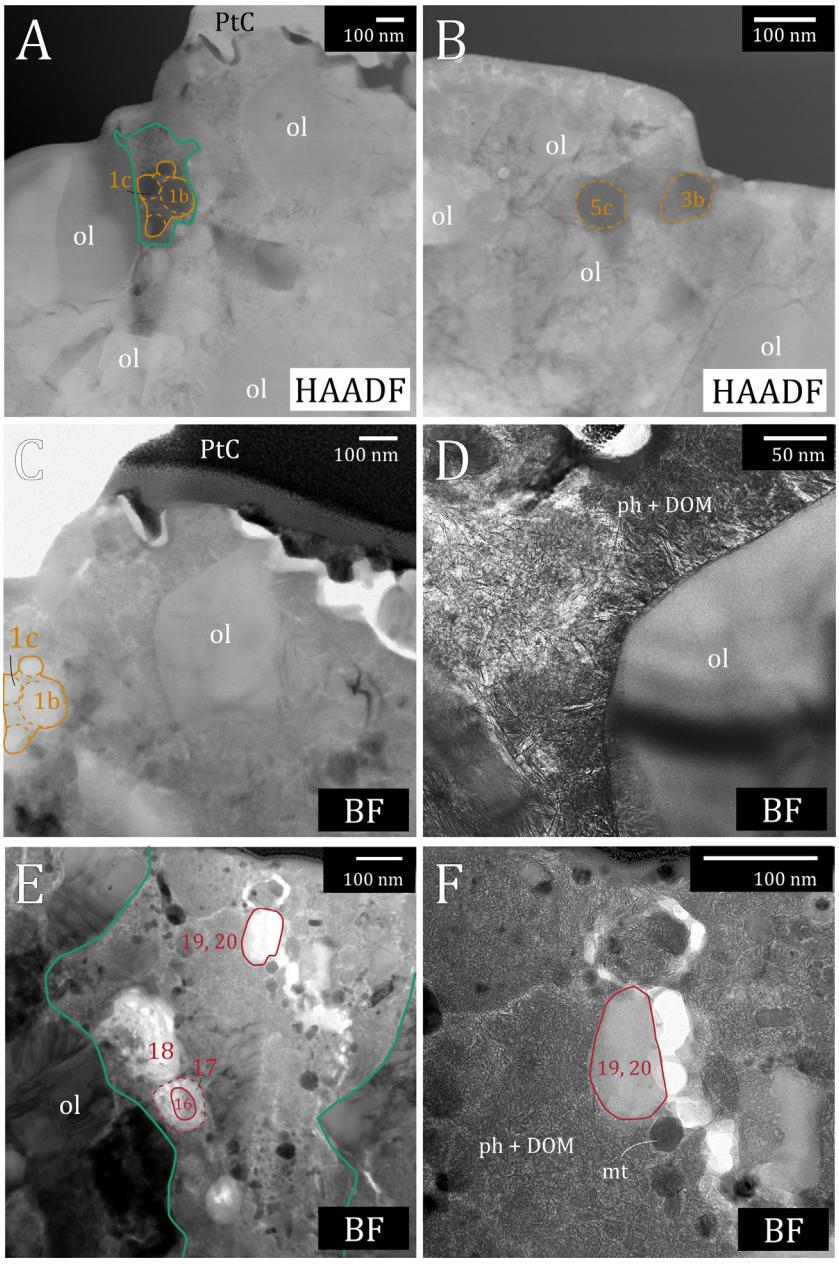

Fig. 3. Bright Field (BF) and High-Angle Annular Dark Field (HAADF) STEM images from A-clast FIB-sections B5 (A–D) and A1 (E–F). These regions show pockets and veins of hydrated silicates (green boundaries) surrounded by anhydrous silicates such as olivine and pyroxene. Orange and red boundaries denote organic globules analyzed using EELS (Fig. 8). Panels C and D are zoom-ins of panel A: note the small size of the phyllosilicates (ph) and their overgrowth on the large olivine (ol) in panel D. DOM = diffuse organic matter, mt = magnetite and PtC is the protection layer on the section.

beam will ionize more organic hydrogen (Bonal et al., 2010a; Piani et al., 2012) and since OM is relatively more enriched in deuterium than the phyllosilicate matrix (Alexander et al., 2012), it is likely that this component is observed in results from Briani et al. (2009).

3.3. Morphology and isotope composition of ^{15}N-rich regions

TEM analyses were carried out on ^{15}N-rich domains from two A-clasts (A1, B5) and one H-clast (A3) (see red arrows in Electronic Annex, Figs. S1 and S2). ^{15}N-rich domains in A-clasts consist of vein-like aqueously altered regions with fine-grained nm-sized phyllosilicates, nm-sized magnetite, globular (~100 nm diameter, mostly solid) and non-globular diffuse carbonaceous matter interwoven with phyllosilicates (Fig. 3). Some globules form chains or clusters together within the vein structures, in agreement with observations by Ishii et al. (2009). These vein-like structures are bordered by crystalline regions of Mg-rich olivine and pyroxene. In certain areas, the grain boundaries of the silicates and carbonaceous grains show phyllosilicate overgrowth (Figs. 3d and 4). The morphology of the

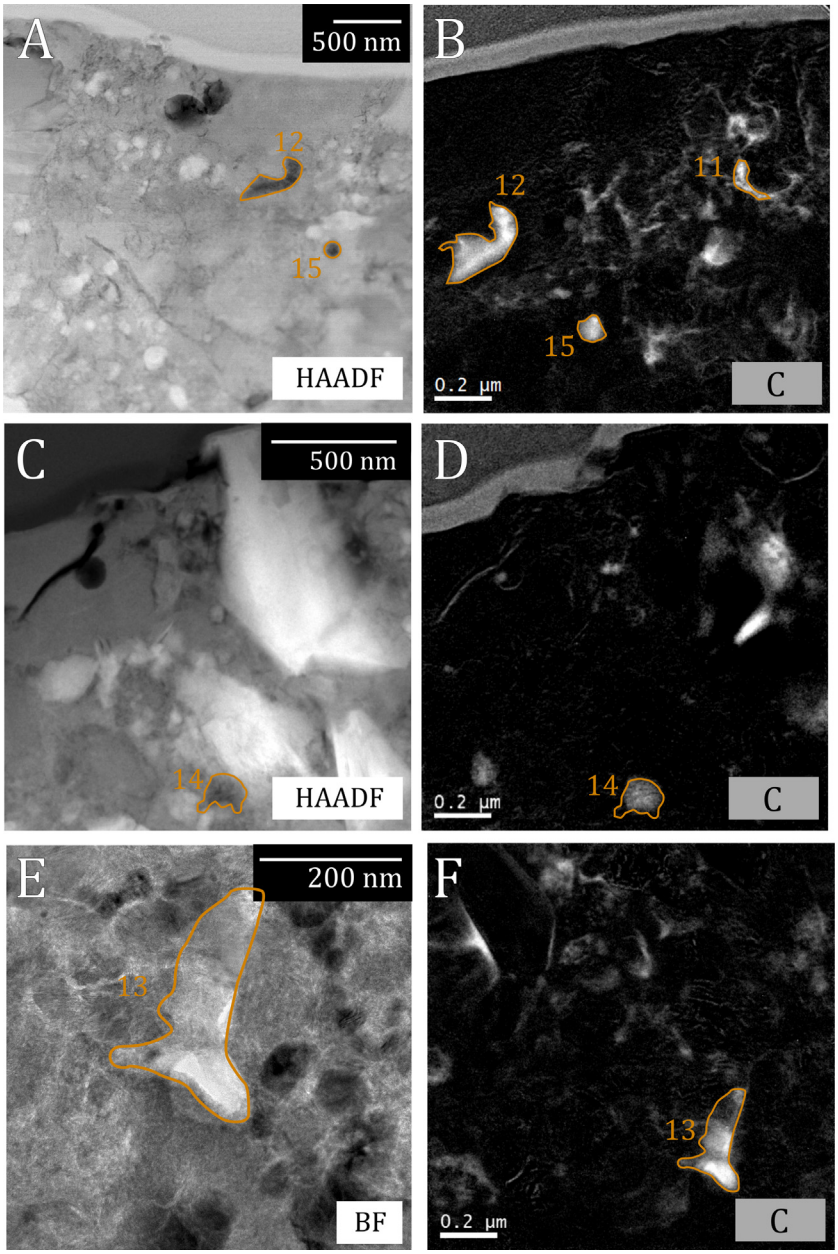

Fig. 4. HAADF-STEM and BF-STEM images from A-clast FIB-section B5 and their respective carbon maps (C) acquired using three-window energy-filtered TEM. These images include more altered organic grains (orange boundaries) analyzed by EELS (Fig. 10), overgrown by phyllosilicates.

H-clast ^{15}N-rich region is distinct from those of A-clasts (Fig. 5). We observe a completely hydrated matrix of more elongated phyllosilicates interspersed with diffuse carbonaceous matter. Large (up to micron sized) Fe-sulfides are embedded in the matrix along with clusters (a few 100 nm in diameter) of carbon-rich matter and Fe-sulfides.

Nitrogen isotope analyses by NanoSIMS were carried out on areas in FIB-sections from one H-clast and one A-clast (A3 and B5, respectively, Fig. 6). Two N isotope image rasters were analyzed in section B5; raster B5(1) was done on a region not analyzed by TEM and raster B5(2) corresponds (on a different scale) to the TEM domain in Fig. 4a. In Fig. 6, $^{12}C^-/^{16}O^-$ and $^{12}C_2^-/^{12}C^{14}N^-$ are shown. Here, for the A-clasts, we observe carbon-rich domains with a globular morphology, which correspond to the nanoglobules observed in the TEM analyses. The detected N isotopes, because of their bonding to $^{12}C^-$ ions (e.g., $^{12}C^{15}N^-$ and $^{12}C^{14}N^-$) are likely derived from carbonaceous matter, but can also be produced from recombined free N- and C-ions. As seen from the $^{12}C^{15}N^-$ over $^{12}C^{14}N^-$ ratio maps in the upper panels, the ^{15}N-rich domains are more or less evenly distributed in the raster images. The globules are on average depleted in ^{15}N relative to the intermediate matter, which consists of carbonaceous

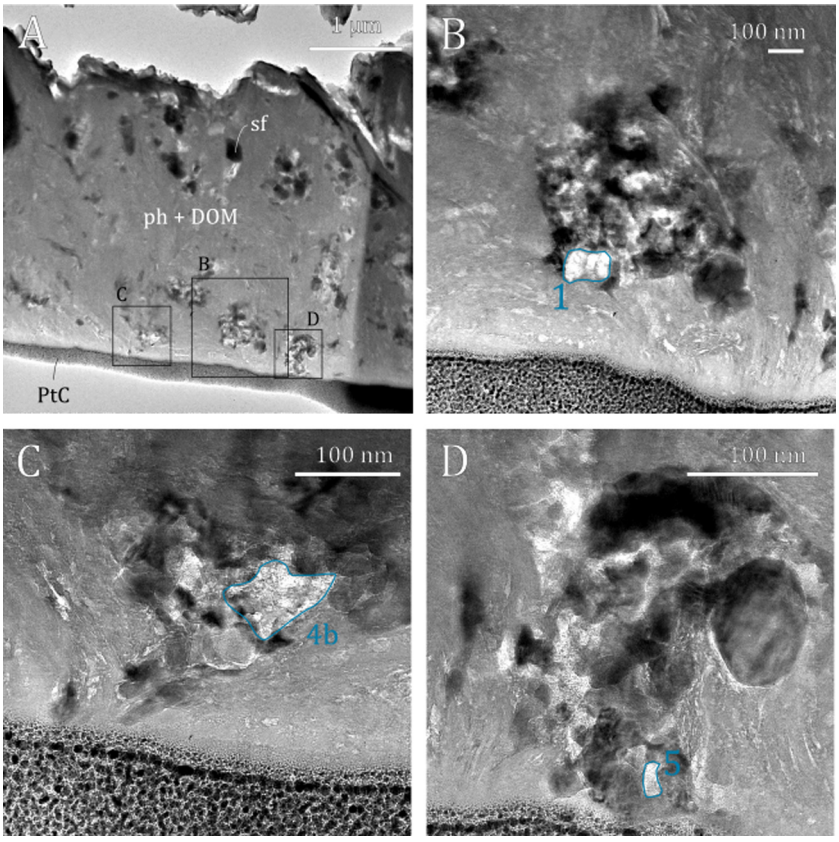

Fig. 5. BFSTEM images from H-clast FIB-section A3. Panel A represents an overview of the section, showing abundant Fe-sulfides (sf) and large phyllosilicate structures. The squares in panel are various zoom-ins of carbonaceous clusters (B–D) that include locations of EELS analyses (blue boundaries, Fig. 7).

matter interwoven with phyllosilicate grains (e.g., diffuse OM). The non-globular area of B5(1) has an average $\delta^{15}N$ value of $1137 \pm 43‰$, whereas the globules are on average less enriched and have a $\delta^{15}N$ value of $885 \pm 22‰$ (Table 5). Some of the domains most enriched in ^{15}N have $\delta^{15}N$ values up to ~5000‰, similar to those observed from the SIMS data. These very enriched domains are populated by the diffuse OM. Similar observations are made for raster B5(2). We note that the ^{15}N-enriched non-globular domain may be occupied by N bound to diffuse OM and/or to free N residing between phyllosilicate layers.

Raster A3 (Fig. 6) represents an H-clast and contains carbonaceous matter clustered together with iron sulfides. BFSTEM images from these regions show that the diffuse carbonaceous material appears to be very finely interwoven with the phyllosilicates on a nm-scale (Fig. 5). The clusters of Fe-sulfide and carbonaceous matter can be a few 100 nm in diameter. The carbonaceous clusters in H-clasts are defined by modest ^{15}N enrichments corresponding to $\delta^{15}N$ values of 105‰ on average, with a range between −300 and 700‰. This is similar to SIMS analyses for bulk ^{15}N values and ^{15}N-rich domains (Table 3). The $\delta^{15}N$ range of diffuse OM cannot be well constrained due to the low count rate of nitrogen in these areas (< 2 counts per pixel for $^{12}C^{15}N^-$). The highest values found for ^{15}N-rich domains by SIMS are <500‰ (Table 3), whereas the NanoSIMS data with a low count rate has hotspot regions of <10000‰. Hence, the NanoSIMS $\delta^{15}N$ average of ≈ 1205‰ for the H-clast diffuse OM is likely overestimated by an order of magnitude, suggesting that the A-clast diffuse OM is more ^{15}N-rich than the H-clast diffuse OM.

3.4. Structural analyses of OM

Electron energy loss spectra (EELS) of C(arbon)-K and N(itrogen)-K edges were obtained for globular and non-globular carbonaceous matter in ^{15}N-rich regions of lithic clasts B5, A1 and A3. Peaks in these spectra are associated with various bonding environments of C and N and, thus, can provide information on the structure of the OM.

3.4.1. H-clasts

The π^* transition in three C–K edges from different carbonaceous clusters in H-clast A3 (Fig. 7) is characterized by a single broad peak at 285 eV, which is indicative of C=C bonding in carbon ring structures. The continuous intensity in this transition suggests that the overall structure of the carbonaceous matter consists of amorphous carbon, which is also supported by characteristic diffuse patterns in electron diffraction. We note that the continuous intensity observed in the π^* transitions of C–K edges may to some

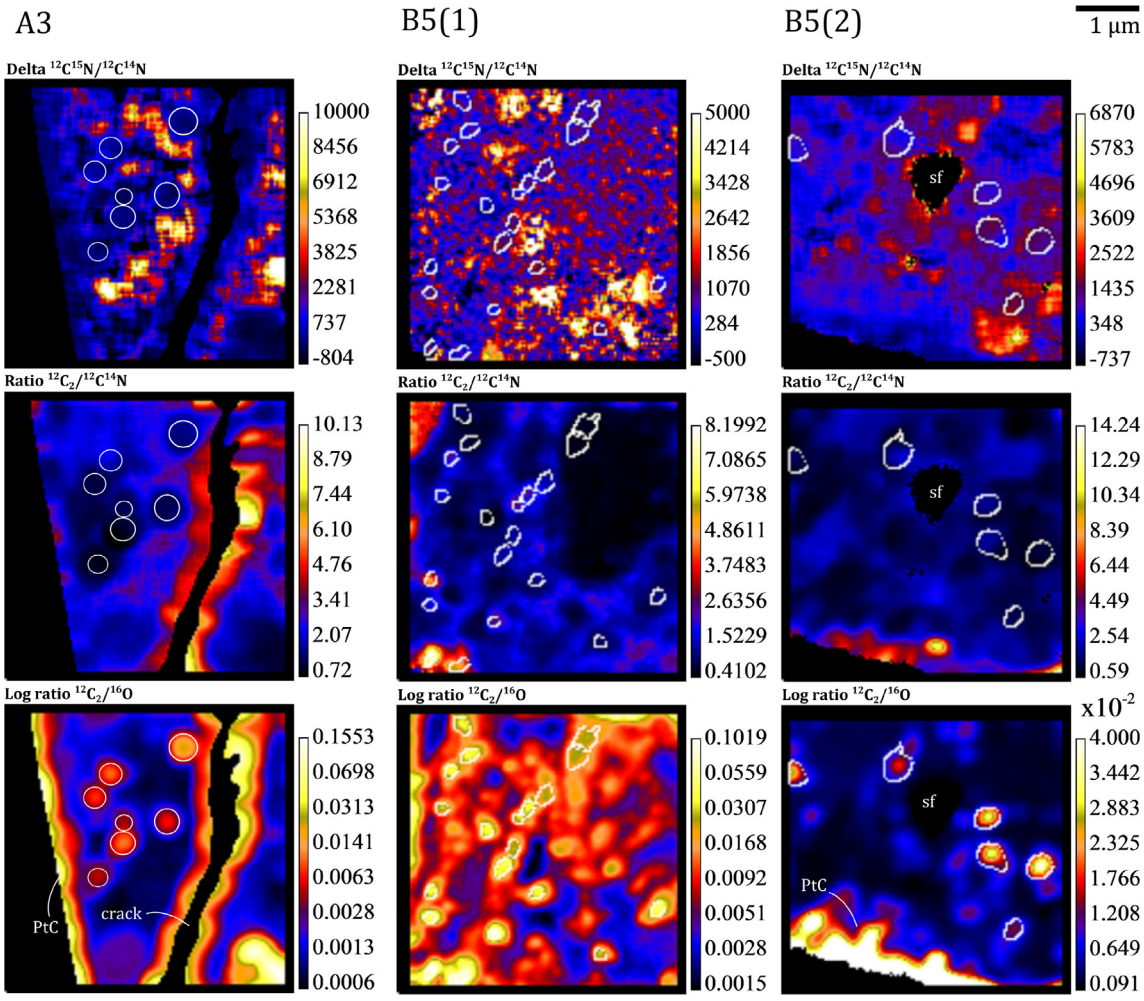

Fig. 6. NanoSIMS raster images for $\delta^{15}N$, $^{12}C_2^-/^{12}C^{14}N^-$ and $^{12}C^-/^{16}O^-$ from three rasters in B5(1), B5(2) and A3. Areas with high $^{12}C^-/^{16}O^-$ ratios represent nanoglobules. These ROIs are overlaid on C^-/CN^- and $\delta^{15}N$ images in white. sf = iron sulfide.

extent be the result of TEM related damage on the section. Degradation of peaks in the π^* transition were previously reported from irradiation experiments on Stardust samples (De Gregorio et al., 2013). However, these experiments were done under extreme conditions (i.e., similar to hyperspectral EDS mapping for long irradiation periods), not representative of our analyses. In addition, we observe no alterations to the sample from post-TEM images and multiple EELS taken from the same area (e.g., A3-4a and A3-4b, Fig. 7; A1–19 and A1–20, Fig. 8) show no significant modifications. Alternatively, the continuous intensities in the C–K edge π^* transitions may be the result of broader peak shapes related to non-ideal sample thickness. However, deconvolution of our C–K spectra to minimize plural scattering does not result in further peak separation.

The N–K egdes presented in Fig. 7 are from the same acquisition as the A3 C–K edges. These spectra show consistently similar features, characterized by an absence of peaks in the 399–402 eV energy range that are related to C–N functionality (C═N bonds in imine at 399 eV, C≡N in nitriles at 400 eV, O═C—N bonds in amido nitrogen at 401.5 eV). We note that the absence of peaks in the 399–403 eV spectral region confirm the lack of radiation damage on our samples, that would have led to a degradation in amine bonds to form C–N environments (Zubavichus et al., 2004). Instead, the N–K edges show broad features between 403–406 eV and between 410–412 eV for all acquired spectra in the section. These peaks lie in a spectral region expected for amine bonds (N–H) in N–heterocycles (i.e., pyrrole and imidazole) (Kebukawa et al., 2013). The absence of C–N functionality suggests that the organic structure likely has amine functional groups attached to carbon ring structures, rather than having N incorporated in the cycles. In Fig. 9, we present H-clast N–K edges together with spectra from organic compounds containing N–H bonding environments. We show that the spectrum from a structure with -NH_2 groups bonded to carbon chains (c in Fig. 9) most closely resembles our data, having similarly broad features in the range of 403–406 eV and 410–412 eV. Alternatively, -NH_2 groups that are connected to carbon ring structures also resemble the H-clast N–K edges (a and b in Fig. 9), suggesting that multiple –NH_2 related structures can cause the observed OM in H-clasts. The lack of C–N bonding environments in H-clast OM is,

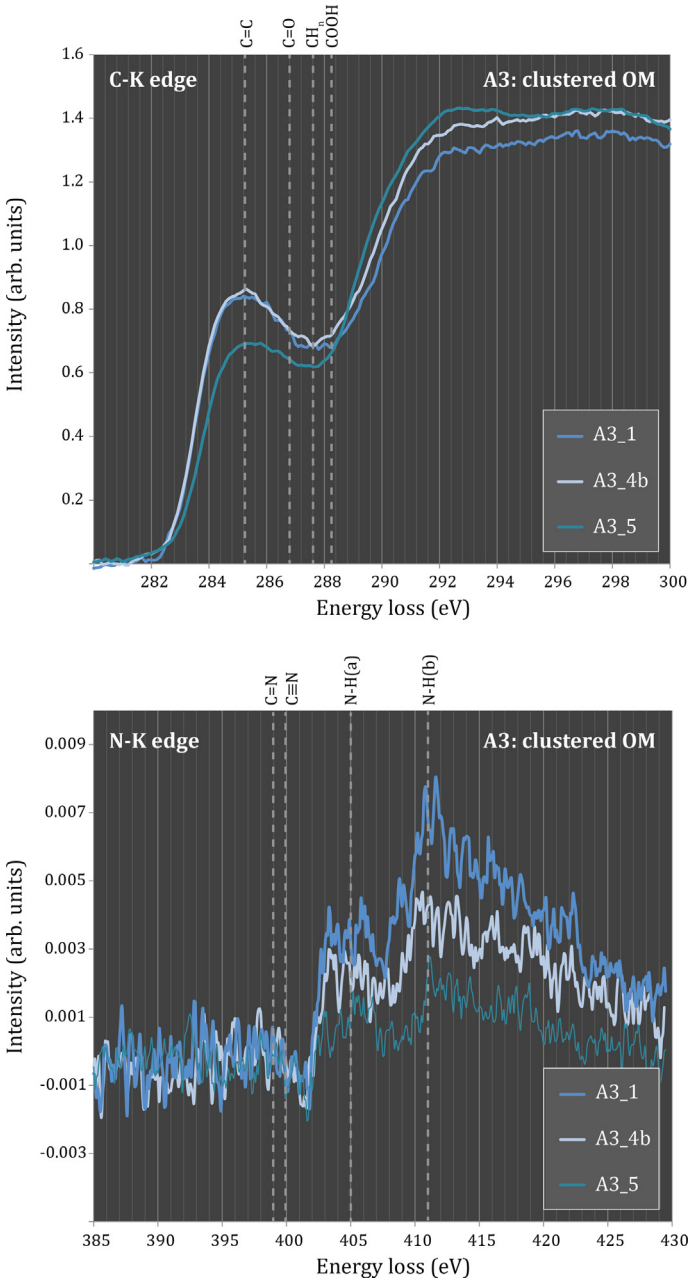

Fig. 7. A stack plot of background subtracted, total carbon normalized C–K-EELS (upper panel) and N-K-EELS (lower panel) from H-clast A3. Peaks in the C–K edges correspond to: 1) (~285 eV) 1s-π^* transition associated with aromatic or olefinic carbon (C=C); 2) (~286.5 eV) 1s-π^* transition associated with carbonyl/ester (C=O) and ether groups (C–O) in aldehydes and ketones, as well as nitrile bonding (C≡N) environments; 3) (~287.5 eV) 1s-3p/σ^* transition associated with aliphatic carbon and 4) (~288.5 eV) 1s-π^* transition associated with carbonyl groups in carboxyl moieties. Peaks in the N–K edges correspond to: (1) (~400 eV) 1s-π^* transition associated with nitrile functional groups (C≡N); 2) The broader peaks between ~403–407 eV [N–H(a)] belong to amine functional groups in imidazole and pyrrole and the broad peak starting at ~411 eV [N–H(b)] is related to amine functional groups in imidazole.

to the best of our knowledge, a unique feature, not observed in other chondritic and cometary OM.

3.4.2. A-clasts

We analyzed multiple globules in FIB-sections from A-clasts B5 and A1. In Fig. 8, we show that the C–K edges for globules in these sections show multiple peaks in the π^* transition, related to aromatic bonds (C=C, 285 eV), aldehyde/ketone/nitrile bonds (aldehyde O=CH, ketone C=O, nitrile C≡N, 286.5 eV), aliphatic bonds (CH_n, 287 eV) and carboxyl bonds (-COOH, 288.5 eV) (peak positions from Cody et al., 2008). Compared to H-clasts, the organic structure of A-clasts globules seemingly incorporates an increased amount of aldehyde/ketone functional groups. Other peaks in the π^* transition corresponding to aromatic, aliphatic and carboxyl functional groups are gen-

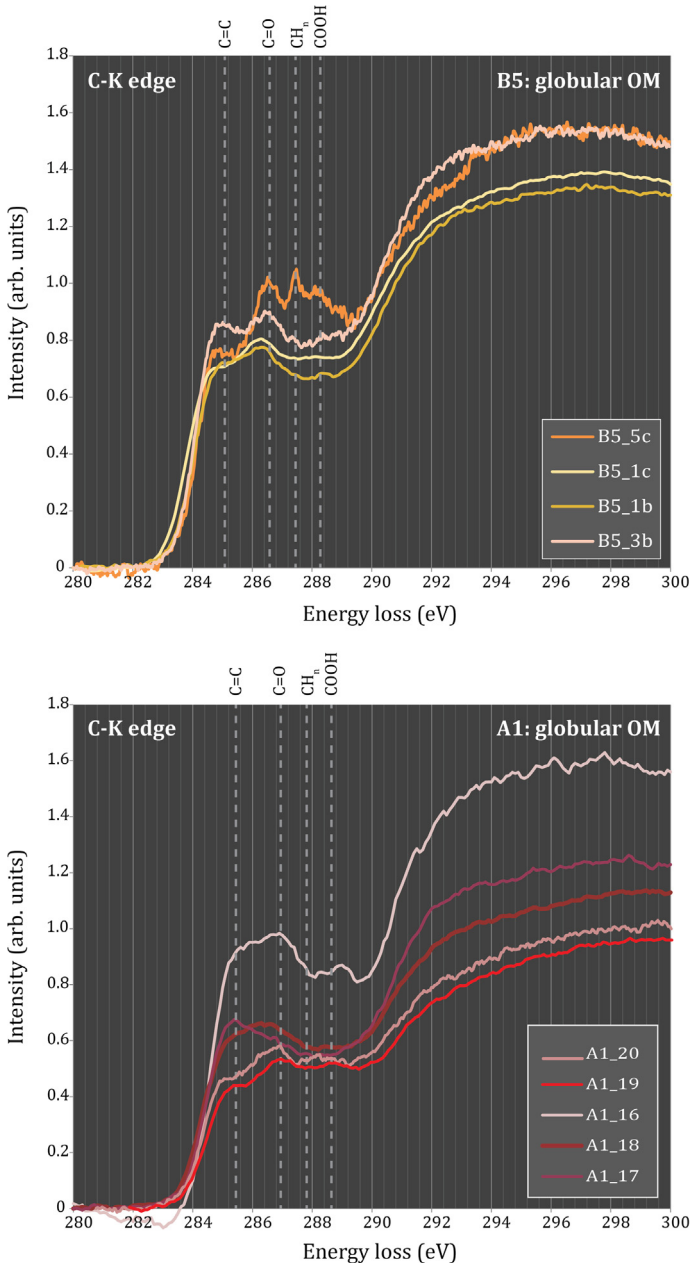

Fig. 8. A stack plot of background subtracted, total carbon normalized C–K-EELS from A-clasts B5 (upper panel) and A1 (lower panel).

erally present to a lesser degree. We observed one globule in section A1 with a core and rim structure, for which we obtained C–K edges (Fig. 8). The core (A1–16) shows an increase in aldehyde/ketone and carboxyl groups compared to the rim (A1–17) that has relatively more aromatic functional groups. The carbon structure of the A-clast nanoglobules generally differs from other carbonaceous chondrites (CR, CM, CI spectra from Le Guillou et al., 2014) by a higher relative intensity of the C=O peak at 286.5 eV in the π^* transition and a lower relative intensity of the COOH peak at 288.3 eV. Cometary IDPs, however, have more in common with A-clasts since IDP carbonaceous matter is moderately aromatic with more intense peaks in the 286.5 eV region (Busemann et al., 2009). In Fig. 10, we present five C–K spectra from OM in section B5 that show clear overgrowth of nanophyllosilicates in BFSTEM and have resolvable N–K edges. We consider this type of OM intermediate between diffuse and globular OM since the organic matter, although overgrown by phyllosilicates, still retains a somewhat globular structure. For these organic grains, we typically observe a decrease in C=O bonding environments relative to the A-clast globules. The calculated C/N ratios range between 20 and 115 and the organic grains seemingly decrease their relative nitrogen content with the solidity of the carbon grain or a lower amount of phyllosilicate overgrowth. The C/N ratios in A-clasts grains are typically higher than found for bulk measurements of carbonaceous chondrites (C/N = 12–22,

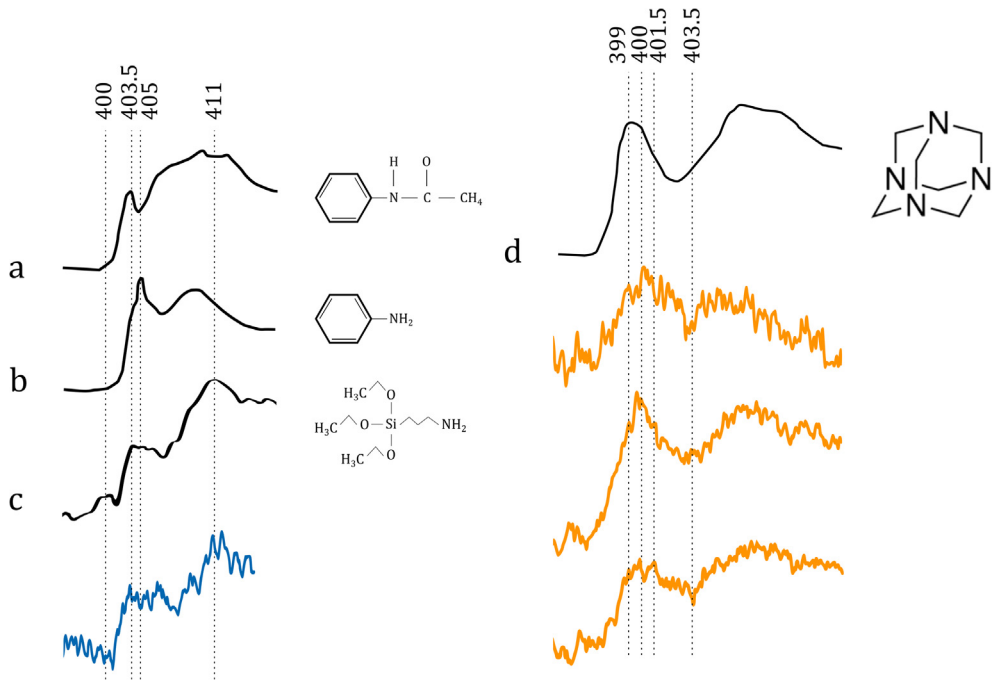

Fig. 9. A comparison of N-K EELS from A- (orange) and H-clasts (blue) with N–K edges from known organic structures. Structures (a) and (b) are data from Franke et al. (1995), (c) is from Iqbal et al. (2014) and (d) is from Keller et al. (2004).

Alexander et al., 2013; Bergin et al., 2015), but are in the same range as insoluble organic residues from these chondrites (C/N ≈ 30 for CI, CM, CR; C/N ≈ 140 for CV, CM; Alexander et al., 2007). We note, however, that the calculation of C/N ratios from EELS data is prone to errors from, for example, background subtraction methods, low counting statistics on the N signal and increases in C/N from radiation damage.

Nitrogen is detected in regions associated with diffuse OM in section B5, and not observed with sufficient signal/noise level in the globules. In contrast to H-clast N–K edges, we find noticeable variations between N–K edges from A-clasts (Fig. 10). In general, the spectra define two broad features, corresponding to (1) C–N bonding environments related to N-heterocycles or nitriles (C≡N) within the 398–402 eV energy range and (2) N–H bonding environments starting at 402.5 eV. Within these broad features we can distinguish smaller peaks, revealing a complex nitrogen chemistry. Four out of five spectra exhibit a more intense broad feature in the C–N region relative to N–H bonding environments, with peak positions at 400 eV that are either related to nitriles (C≡N) or C=N bonds in imidazole (Kebukawa et al., 2013). Less pronounced peaks are observed at 399 eV (imine nitrogen) and 401.5 eV (amido nitrogen). One spectrum (B5–13) has a more noticeable peak at 401.5 eV and a C–N broad feature with lower intensity than found for the N–H broad feature, suggesting a relatively higher abundance of N–H bonding environments compared to the other B5 spectra. In all spectra, we observe a low at 403.5 eV, where we would expect urea nitrogen. Comparing our spectra to known organic compounds shows that B5 N–K edges most closely resemble hexamethylenetetramine ($C_6H_{12}N_4$), a structure defined by N incorporated in heterocycles (Fig. 9d, Keller et al., 2004). However, our spectra are favoured by nitrile over imine bonds. Next to EELS and XANES obtained from chondritic and cometary organics, our B5 spectra most closely resemble IDPs L2005*A3 and L2011R11 (Keller et al., 2004). Collectively, B5 N–K edges show that C–N bonding environments play a dominant role in the nitrogen chemistry of diffuse OM in A-clasts.

In summary, the carbon bonding environments in H-clast and A-clasts differ distinctly in their C=O functionality, which is more pronounced for A-clasts. Additionally, A-clasts exhibit smaller peaks related to aliphatic and carboxyl functional groups and have, based on our observations, increased aromatic functionality in globule rims relative to their cores. Additional variations in these spectra may be obscured by damage obtained during TEM observations or non-ideal sample thickness. Finally, we find clear differences between N–K edges from H- and A-clasts, which exhibit amine and nitrile bonding environments, respectively.

3.5. Mg and Cr isotopes

We present Mg and Cr isotope measurements of H- ($n = 6$) and A-clasts ($n = 3$) in Table 4. Previous analyses were carried out solely on H-clasts together with bulk samples and components of other metal-rich carbonaceous chondrites (Van Kooten et al., 2016). This study showed that these meteorites have a distinct signature in Mg and Cr isotope space from other Solar System objects including ordinary and enstatite chondrites, carbonaceous chondrites (CI, CM, CO, CV, CK) and terrestrial planets. In detail,

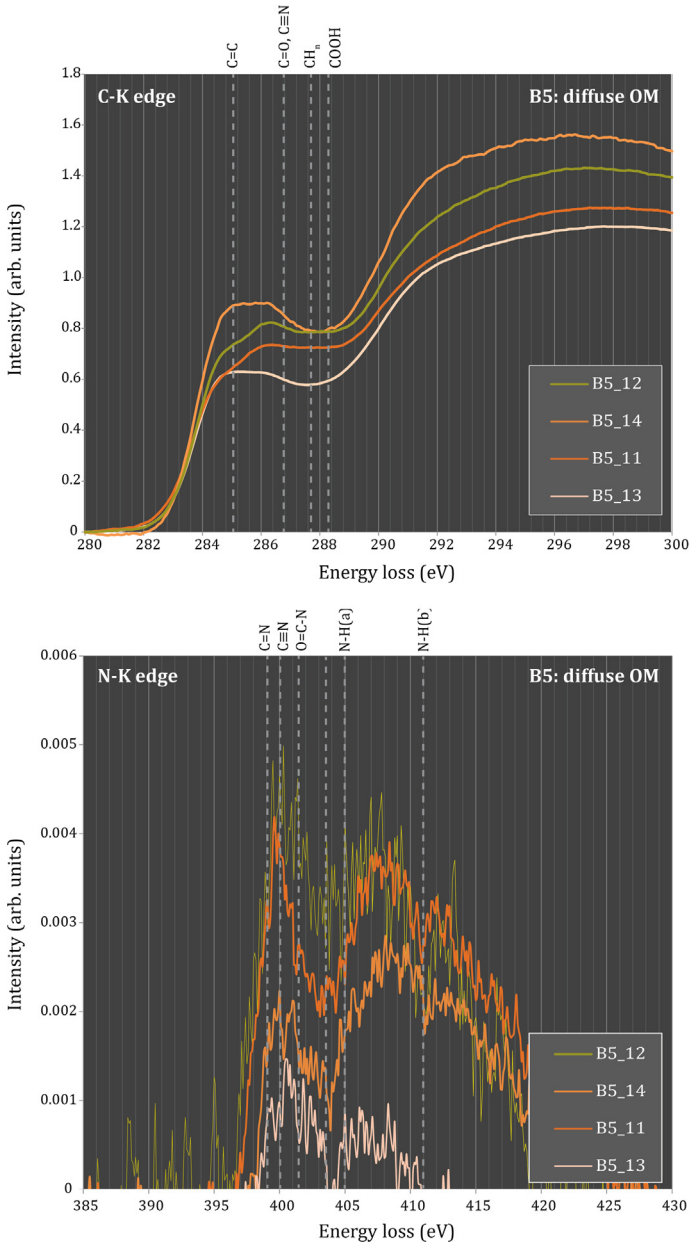

Fig. 10. A stack plot of background subtracted, total carbon normalized C–K-EELS (upper panel) and N-K-EELS (lower panel) from altered OM in A-clast B5.

metal-rich carbonaceous chondrites and their components define an array extending from an inner Solar System composition akin to CM chondrites towards a $^{26}Mg^{*}$-depleted and ^{54}Cr-enriched endmember (Fig. 11). This array is interpreted to represent a reservoir that was spatially isolated from planetary and asteroidal bodies plotting on the inner Solar System correlation line (Larsen et al., 2011). The combined Mg and Cr isotope signatures of Solar System objects can, thus, be used to determine their accretion regions. Our new ^{54}Cr and $^{26}Mg^{*}$ data include A-clasts, which overlap in Mg and Cr isotope space with H-clast and CR chondrite compositions (Van Kooten et al., 2016; Table 4). However, on average, A-clasts appear more enriched in ^{54}Cr than H-clasts (Fig. 12).

4. DISCUSSION

4.1. Multiple organic precursors from Isheyevo lithic clasts

4.1.1. Evidence from H isotope data

Hydrogen isotope measurements of meteorites can be acquired through various methods, thereby extracting information on the D/H composition of different components and scales. For example, digestion of whole rock samples and subsequent analyses of leachates by gas mass spectrometry provides a different range of information relative to *in situ* SIMS and NanoSIMS measurements. Our bulk H isotope analyses on various Isheyevo lithic clasts provide data on the D/H signature of the -OH component

Table 4
Magnesium and chromium isotope data for clasts extracted from the Isheyevo meteorite, including H-clasts and A-clasts, as well as a CI-type chondritic lithic clast. n = number of analyses per sample. The error is presented as 2SE.

	$^{27}Al/^{24}Mg$	μ^{26} Mg* (ppm)	μ^{25} Mg (ppm)	n	$^{55}Mn/^{52}Cr$	μ^{54} Cr (ppm)	n
H-clasts							
A2-LC-1†	0.096	−7.8 ± 5.7	−110 ± 6	5	1.19	117 ± 18	7
A2-LC-2†	0.115	−8.9 ± 5.5	−2 ± 6	10	0.57		
A2-LC-3†	0.092	−7.9 ± 3.5	−56 ± 5	10	0.90	142 ± 28	5
B4-LC-1†	0.086	−8.1 ± 3.4	−186 ± 8	5	2.30		
B4-LC-BC†	0.093	−3.5 ± 2.6	−77 ± 6	10	1.46	117 ± 2	6
CdLC2	0.100	−3.6 ± 5.0	−114 ± 6	10	1.84	119 ± 8	16
A-clasts							
DLC4	0.096	0.7 ± 5.3	−99 ± 9	10	0.75	141 ± 7	16
DLC6	0.102	−4.9 ± 3.8	−122 ± 7	10	0.69	138 ± 14	15
B3_1*	0.102	−7.3 ± 3.6	−181 ± 4	10	0.49	135 ± 6	16
CI							
CdLC3	0.096	4.1 ± 5.0	−232 ± 7	10	0.87	166 ± 6	16

† Analyses are done by Van Kooten et al. (2016).
* Analyzed for N- and H-isotopes.

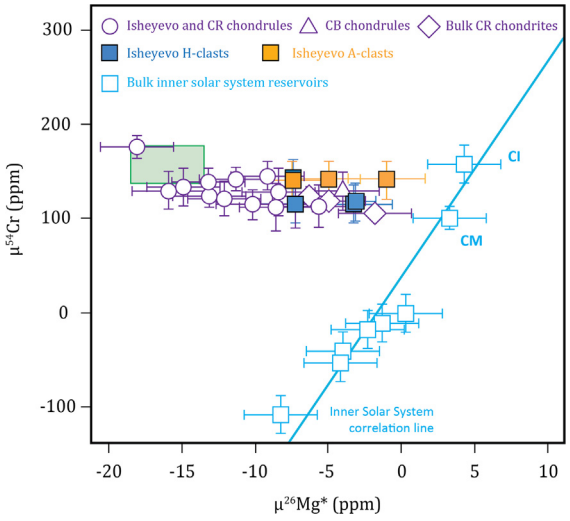

Fig. 11. The ε^{54}Cr and $\mu^{26}Mg^*$ compositions of metal-rich chondrites and their components as well as bulk inner Solar System reservoirs. This figure is modified after Fig. 2 in Van Kooten et al. (2016) to include individual H- and A-clasts. Uncertainties reflect the external reproducibility or internal errors, whichever is larger. Some of the ε^{54}Cr uncertainties are smaller than symbols. The green box represents the predicted ε^{54}Cr and $\mu^{26}Mg^*$ compositions of the ^{26}Al-free and thermally unprocessed molecular cloud material, including their uncertainties. The plotted compositions of CB chondrules represent averages of individual samples.

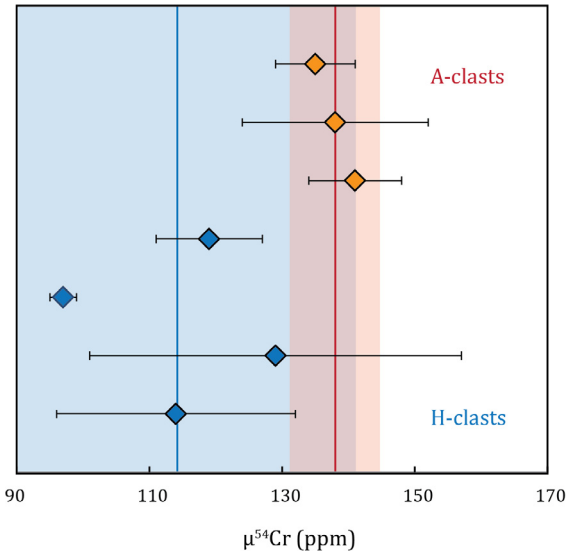

Fig. 12. ε^{54}Cr data from individual H- and A-clasts presented with a 2SE error. Averaged data for both clast types is represented by blue and red bars with a 2SD error.

in phyllosilicates from the matrices of these clasts. The use of an O^- primary beam significantly minimizes the contribution from organic derived hydrogen. However, the D/H signature of the water bound to the phyllosilicates is thought to represent a mixture of hydrogen derived from organics and/or their precursors and from the fluid that altered the initial silicates (i.e., amorphous silicates, olivines and pyroxenes) present in the matrix (Alexander et al., 2012). The fluid itself is derived from a mixture of H-bearing icy components (e.g., H_2O, NH_3, HCN) that were molten during heating of the parent body. Hence, D/H compositions of phyllosilicates can be used to extract information about the endmember components of aqueous alteration processes, such as organic precursors.

We plot in Fig. 13 the H isotope data of phyllosilicates in five H-clasts (blue) and five A-clasts (orange) against their $^{28}Si^+/H^+$ count ratios, which is used to express variability in δD composition associated with progressive hydration of the clasts. The Si^+/H^+ ratio is used here as a relative measure for the amount of hydration in phyllosilicates and should not be confused with absolute ratios. Similarly, Alexander et al. (2012) have previously plotted bulk δD compositions against C/H ratios in carbonaceous chondrites to infer a D/H endmember compositions of water, assuming a common endmember for chondritic IOM. They

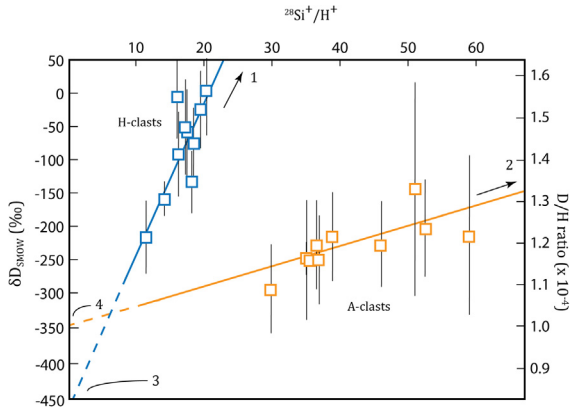

Fig. 13. Plot of $^{28}Si^+/H^+$ against δD_{SMOW} (‰) for Isheyevo lithic clasts. A decrease in Si^+/H^+ signifies an increase in relative water content. Blue and orange squares represent H-clasts and A-clasts, respectively. Error bars define 2σ. Best fit linear correlations are plotted, with a mean square weighted deviation (MSWD) of 1.7 for H-clasts and MSWD = 0.3 for A-clasts. Linear correlations intersect with Si/H = 0 at '3' for H-clasts ($\delta D = -450$‰) and '4' for A-clasts ($\delta D = -350$‰), corresponding to the highest relative water content. The other ends of the hydration lines are defined by '1' and '2' and correspond to the lowest relative water content with relatively high δD.

noted that the bulk C/H composition of chondrites is dependent on soluble OM and carbonates in addition to IOM, which may explain to some extent the scatter in aqueous alteration trends of bulk chondrites. Here, we use the Si^+/H^+ ratio that reflects a constant contribution of Si from the initial silicates, assuming no additional Si from the altering fluid, and an increasing amount of H added from the fluid relative to the organics. Both H- and A-clasts show a decrease in their δD values with progressive hydration, defining two different populations (Fig. 13). In detail, the two clast populations define distinct correlations between D-poor components (see component 3 and 4 in Fig. 13) and two varying D-rich endmembers (H-clasts: 1, A-clasts: 2). We suggest that these correlations reflect a decrease in D/H with increasing hydration of variable D-rich OM with D-poor fluid(s). This interpretation is contradictory to a previously proposed common organic precursor for chondrites and comets (Alexander et al., 2012). It is unlikely that the correlations between δD and Si^+/H^+ in Isheyevo lithic clasts are related to matrix effects, since δD ratios from both chrysotile and antigorite standards are unaffected by changes in Si^+/H^+ (Fig. 14). Additionally, H-clasts exhibit larger variations in δD, whereas they have a mineralogy that is less susceptible to matrix effects compared to A-clasts: H-clasts contain only silicates in hydrated form, whereas A-clasts contain a mixture of hydrated and anhydrous silicates. Deloule and Robert (1995) showed that the main control on matrix effects for H isotopes is the electronegativity of the octahedral site in hydrated silicates, which is affected by substitution of Mg by Fe. However, since the fractionation factors observed for our antigorite (Fe-rich) and chrysotile (Mg-rich) reference standards are very similar (see Section 2.4), the effect on the D/H ratio of our samples is typically within the uncertainty of our measurements. Also, the Fe/Mg compo-

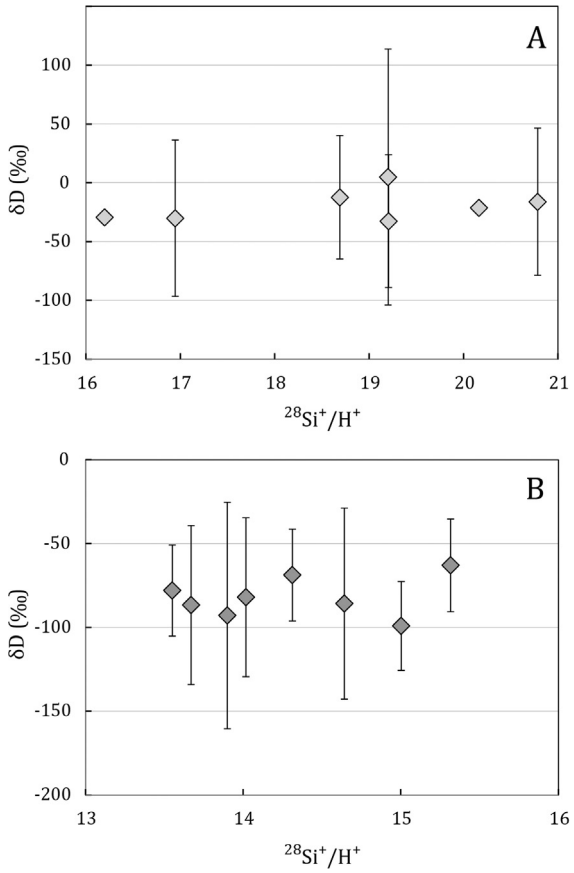

Fig. 14. Plots of $^{28}Si/H$ against δD_{SMOW} derived from endmember phyllosilicate compositions of antigorite (A) and chrysotile (B) used as standards for H isotope measurements of Isheyevo lithic clasts. Average δD values for antigorite ($\delta D = -33 \pm 17$) and chrysotile ($\delta D = -84 \pm 17$) are in agreement with literature data (Alt and Shanks, 2006). Note that no variation of δD with Si/H is observed for these standards, implying that matrix effects influenced by changes in this ratio are not detectable.

sitions of A-clast and H-clast phyllosilicates completely overlap (Fig. 1), again suggesting that matrix effects are not the cause of the observed H isotope variations. Furthermore, we can rule out shock-induced isotope fractionation, since the absence of mineral fractures, local melting or foliations in the lithic clasts excludes this process as a relevant mechanism (Bonal et al., 2010b). Alexander et al. (2012) proposed an increase of D/H in chondritic water reservoirs (e.g., CR and ordinary chondrites) as a result of Fe oxidation during aqueous alteration. However, the D-rich component in ordinary chondrites has recently been identified as thermally recalcitrant (Remusat et al., 2016), whereas metal in CR chondrites have experienced a minimal amount of oxidation (Wasson and Rubin, 2010). Hence, it is unlikely that the D/H ratios measured in metal-poor H-clasts are affected by Fe oxidation. In sum, we have established that the OM present in the clasts does not reflect a variable degree of hydration of a common precursor (Alexander et al., 2012). Rather, the two trends defined by the clasts are consistent with the progressive hydration of two distinct organic precursors by D-poor water reservoirs of slightly different compositions.

To constrain the D-rich endmember compositions, we have calculated the absolute phyllosilicate water content from measured $H^+/^{30}Si^+$ ratios based on the stoichiometry of our chrysotile standard. Hydrogen isotope signatures of D-rich endmembers from A-clast and H-clast mixing arrays can be inferred from mixing hyperbolae in a δD versus H_2O content diagram (Fig. 15), by extrapolation of a power law function. Although the narrow range of data makes it difficult to constrain the mixing hyperbolae, their strong curvature is in accordance with the concentrations of hydrogen in the D-rich endmembers (e.g., organic precursors with relatively low H concentrations) and the D-poor endmember (e.g., a fluid consisting mainly of water). We note that comparing the calculated water content of our Orgueil standard (7.70 wt%, Table 3) to literature (Alexander et al., 2012; Garenne et al., 2014; King et al., 2015) results in an underestimation of 1–10 wt% and, hence, the H_2O contents of these clasts are probably too low as well, suggesting that the D/H endmember signatures may be less depleted than estimated from Fig. 15. From Fig. 15, we find the fluid endmember signature (100% H_2O) to have a δD value of >-600‰. This relatively low D/H ratio is likely caused by thermal processing resulting in isotopic equilibration between ISM derived D-rich H_2O and D-poor H_2 gas in the inner Solar System (Cleeves et al., 2014). The H isotope composition of this water component in H- and A-clasts is akin to other carbonaceous chondrites such as CI and CM chondrites (Fig. 2), which may indicate a similar accretion region. Alternatively, a D-poor reservoir may also exist at larger orbital distances due to recycling of thermally processed inner Solar System material (Yang et al., 2013). Indeed, Jupiter Family comets that likely accreted in the Kuiper Belt at distances >50 AU (Brownlee et al., 2012) can exhibit Earth-like D/H signatures (Hartogh et al., 2011, with the exception of 67P/Churyumov–Gerasimenko, Altwegg et al., 2015). The signatures of the two organic precursors are difficult to estimate, because the vertical asymptotes of the mixing hyperbolae approach infinity. We estimate lower limits for the organic precursors of >300‰ for A-clasts and >2000‰ for H-clasts. While these estimates may be uncertain, we note that the organic precursor material in H-clasts is likely more D-rich than that of A-clasts.

It has recently been suggested that carbonaceous chondrites accreted small proportions of thermally labile D-rich organic radicals to their IOM, resulting in a bulk IOM δD of ≈800‰ for CI chondrites (Remusat et al., 2009; Remusat et al., 2016). Ordinary chondrites, on the other hand, acquired a very small portion of extremely D-rich and thermally recalcitrant organic moieties, resulting in very enriched bulk IOM δD values of ≈3000‰. The presence of at least two variable D-rich organic precursor components in Solar System objects is in agreement with our results.

4.1.2. Evidence from N isotope data

In Fig. 16, we have plotted the NanoSIMS derived $\delta^{15}N$ values of nanoglobules/carbonaceous clusters (circles) and diffuse OM (squares) from H-clasts (blue) and A-clasts (orange) against their respective $^{12}C_2^-/^{12}C^{14}N^-$ ratios (see also Table 5), where the $^{12}C_2^-/^{12}C^{14}N^-$ ratio is a proxy for the C/N ratio. In this space, our data plot in a triangle shaped region suggesting at least three endmember

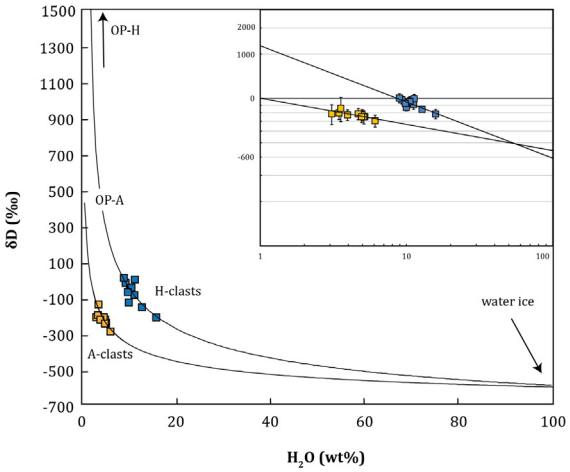

Fig. 15. Plot of H isotope data in delta notation versus the calculated phyllosilicate water content (see text for further explanation) for Isheyevo lithic clasts. Data is also shown as log–log plot in box. For both clast types mixing hyperbolae are fitted between water ice endmember (100% H_2O) and a D-rich organic precursor (OP) endmember using a power law, with $R^2 = 0.65$ for H-clast data points and $R^2 = 0.59$ for A-clasts. The water ice has a estimated composition of ~ −600‰ and the organic precursors are D-rich with OP-A > 300‰ and OP-H > 2000‰. The water content of the lithic clasts is probably underestimated, based on the calculated water content of our Orgueil standard from chrysotile stochiometry. As a result, the endmember compositions are likely more enriched in D/H. Note that these estimations are approximations and meant to indicate the relative enrichments and depletions between different OM precursors and the initial water ice in the lithic clasts.

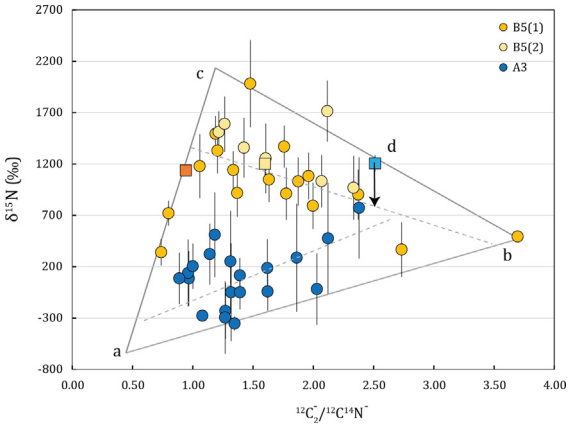

Fig. 16. Plot of $\delta^{15}N$ versus $^{12}C_2/^{12}C^{14}N$ from NanoSIMS data. Circles represent data from globules from A-clasts (orange) and clusters with carbonaceous matter and sulfides from H-clasts (blue). The squares are diffuse OM. The data is confined in a triangular area defined by components a, b and c. Component 'd' may represent an additional endmember composition. The dotted lines represent regressions through the globules of H-clasts (MSWD = 7.1) and A-clasts (MSWD = 4.0). The large scatter in these data suggest that H- and A-clasts accreted components a-d to different extent.

Table 5
NanoSIMS data from TEM sections B5 (A-clast) and A3 (H-clast). Regions of interest (ROIs) are nanoglobules defined by their C/O ratios (see also Fig. 6). Errors are given as 2SE.

Sample	δ^{15}N (‰)	C/CN	Sample	δ^{15}N (‰)	C/CN
B5–3#1			*A3-2#1*		
Diffuse OM	1137 ± 43	0.94 ± 0.00	Diffuse OM	1205 ± 81	2.51 ± 0.01
ROI 1	902 ± 243	2.37 ± 0.03	ROI 1	186 ± 282	1.62 ± 0.03
ROI 2	1329 ± 221	1.21 ± 0.01	ROI 2	85 ± 266	0.97 ± 0.02
ROI 3	1140 ± 185	1.34 ± 0.01	ROI 3	476 ± 540	2.12 ± 0.07
ROI 4	793 ± 225	2.00 ± 0.02	ROI 4	511 ± 412	1.18 ± 0.03
ROI 5	340 ± 129	0.74 ± 0.01	ROI 5	137 ± 326	0.96 ± 0.03
ROI 6	1049 ± 218	1.63 ± 0.02	ROI 6	250 ± 492	1.31 ± 0.05
ROI 7	366 ± 265	2.73 ± 0.04	ROI 7	−50 ± 476	1.32 ± 0.05
ROI 8	720 ± 121	0.80 ± 0.01	ROI 8	288 ± 527	1.86 ± 0.06
ROI 9	911 ± 255	1.78 ± 0.02	ROI 9	−353 ± 69	1.35 ± 0.01
ROI 10	1178 ± 309	1.06 ± 0.02	ROI 10	−278 ± 44	1.08 ± 0.00
ROI 11	492 ± 165	3.70 ± 0.03	ROI 11	114 ± 172	1.39 ± 0.02
ROI 12	1492 ± 175	1.19 ± 0.01	ROI 12	−42 ± 188	1.62 ± 0.02
ROI 13	1368 ± 204	1.76 ± 0.01	ROI 13	−50 ± 166	1.39 ± 0.02
ROI 14	1082 ± 228	1.96 ± 0.01	ROI 14	203 ± 220	1.00 ± 0.02
ROI 15	917 ± 232	1.37 ± 0.01	ROI 15	322 ± 296	1.14 ± 0.02
ROI 16	1030 ± 235	1.88 ± 0.01	ROI 16	772 ± 493	2.38 ± 0.06
ROI 17	1981 ± 424	1.48 ± 0.01	ROI 17	−19 ± 347	2.03 ± 0.05
			ROI 18	−231 ± 272	1.27 ± 0.03
B5 3#2			ROI 19	86 ± 250	0.89 ± 0.02
Diffuse OM	1209 ± 64	1.60 ± 0.01	ROI 20	−295 ± 353	1.27 ± 0.04
ROI 1	1510 ± 201	1.22 ± 0.01			
ROI 2	1713 ± 298	2.12 ± 0.03			
ROI 3	1033 ± 255	2.07 ± 0.03			
ROI 4	968 ± 311	2.33 ± 0.04			
ROI 5	1358 ± 292	1.43 ± 0.02			
ROI 6	1254 ± 340	1.61 ± 0.03			
ROI 7	1589 ± 269	1.27 ± 0.02			

components. Component (a) is defined by a relatively low C/N ratio and a low δ^{15}N value that is similar to the proto-solar gas reservoir as determined by the solar wind (δ^{15}N ≈ −440‰; Marty et al., 2010a). Component (b) has a relatively higher C/N ratio and is moderately enriched in δ^{15}N by about +400‰ (upper limit) and component (c) is with an intermediate C/N ratio, very enriched in δ^{15}N, with a lower limit value of ≈2200‰. If we view the distribution of data points in this triangular area, we may consider more than three endmembers. To some extent (MSWD = 7.1 for a linear fit), the H-clast organic clusters in Fig. 16 seem to correlate positively with their C/N ratios towards the composition of H-clast diffuse OM. These data can be viewed as a two-component system, with endmember components (a) and (d), the latter consisting of diffuse OM with moderately high δ^{15}N and C/N. In contrast, the nanoglobules from both A-clast sections describe an array with a negative slope parallel to the line connecting components (b) and (c) [MSWD = 4.0 for a linear fit of B5(1)]. Two nanoglobules from B5(1) plot between B5(1) diffuse OM and component (a). Within the analytical uncertainties of our measurements (i.e., depending on the definition of our region of interest), we suggest the diffuse OM to be the ^{15}N-rich endmember of the A-clast array. We consider this to be very likely, because the most extreme ^{15}N-rich regions are covered by non-globular matter (Fig. 6). Similar to our H isotope data, we can interpret the H- and A-clast arrays as mixing between a fluid component and an organic component. Notably, the C/N ratio of the fluid is not necessarily lower than that of the organic precursors, since the fluid may be composed of similar organic solvents and the organic precursors may have formed in different temperature regimes (see for further discussion Sections 4.1.4 and 4.1.5). Here, we interpret the composition of the diffuse OM as a proxy for the altering fluid, since (1) diffuse OM is texturally related to hydrated silicates and (2) it has been suggested that diffuse OM is similar in composition to SOM (Le Guillou et al., 2014). In our scenario, the organic precursor of the H-clasts has a relatively low C/N and is depleted in ^{15}N similar to the solar gas composition (component a). The A-clasts organic precursor has a higher C/N ratio and is more enriched in ^{15}N with an upper limit of +400‰ (component b). Furthermore, our combined SIMS and NanoSIMS N isotope data suggest that the diffuse OM from A- and H-clasts have different δ^{15}N values as well as contrasting C/N ratios. From the scatter in our data, specifically the A-clast nanogobules plotting between A-clast diffuse OM and component (a), we suggest that the components described above are not singular to either type of clast, but may be mixed to different extents in the accretion regions of these objects. Collectively, we propose that the organic precursors of H- and A-clasts are relatively

^{15}N-poor ($\delta^{15}N_H = -400‰$, $\delta^{15}N_A = <+400‰$) compared to their respective fluid components ($\delta^{15}N_H = \ll 1200‰$, $\delta^{15}N_A = >1200‰$).

4.1.3. Heritage of organic precursors from their H and N isotope signatures

We infer from isotope data of Isheyevo lithic clasts that variations in N and H isotopes are consistent with the accretion of multiple organic precursors and subsequent alteration by fluids with different (isotopic) compositions. The OM accreted in A-clasts is suggested to be moderately D- and ^{15}N-rich, whereas H-clast OM is very D-rich and extremely ^{15}N-poor, similar to the protosolar $^{15}N/^{14}N$ ratio (Marty et al., 2010b). Correlated D and ^{15}N enrichments as inferred from A-clast OM are indicative of ion–molecule reactions occurring in cold ($T < 10$ K), dense environments as found in molecular clouds (Rodgers and Charnley, 2008; Aléon, 2010; Wirström et al., 2012) or related to N_2 self-shielding occurring in dense molecular cloud cores (Clayton, 2002; Lyons, 2009; Heays et al., 2014). A D-rich organic component, anti-correlated with ^{15}N, can be explained by ion-molecule reactions that occur at higher temperatures (10 K $< T <$ 70 K; Millar et al., 1989). At these temperatures, D/H fractionation in hydrocarbons amongst others is still efficient ($D/H \approx 10^{-2}$). Alternatively, recent investigations that are dedicated to experiments and models describing the formation of organic molecules in the protoplanetary disk show that irradiation-induced reactions can result in significant ^{15}N- and/or D-enrichments (Remusat et al., 2006; Chakraborty et al., 2014; Heays et al., 2014; Kuga et al., 2015; Laurent et al., 2015; Cleeves et al., 2016). It is clear that under certain disk conditions, the requirements from ^{15}N and/or D enriched hotspots in chondritic organics are met. For example, UV irradiation experiments show that carbonaceous polymers such as benzylic carbon can be enriched in δD up to 1250‰ (Remusat et al., 2006; Laurent et al., 2015), although these experiments cannot reproduce the extreme D enrichments observed in ordinary and CR chondrites (Remusat et al., 2006; Alexander et al., 2007). Moreover, irradiation of nitrogen gas shows that extreme enrichments in ^{15}N (^{15}N = 2000–10,000‰) could be achieved within the surface layers of protoplanetary disks (Chakraborty et al., 2014). However, as suggested by Cleeves et al. (2016), the entire carbon budget of the disk must be taken into account to meet the requirements of the carbonaceous matter in chondrites. Thus, in order to constrain these models further, a more detailed knowledge of the disk's physical properties (e.g., ionization potential, density) is required. Furthermore, investigations of how H and N chemical networks operate together in a disk environment are still in their early stages (Roueff et al., 2015). Collectively, purely from a carbon budget point of view, we argue for an interstellar or molecular cloud heritage of D-rich and D-^{15}N rich OM in H- and A-clasts. During the protostellar phase, these organic precursors may be further processed under different temperature regimes, resulting in varying N and H isotope signatures. From an isotopic perspective, the H-clast organic component resembles D-rich/^{15}N-poor organic moieties from ordinary chondrites, which are suggested to contain small contributions from the ISM (Remusat et al., 2016). The inferred A-clast organic endmember composition, on the other hand, shows more resemblance to correlated D-^{15}N enrichments found in IOM from carbonaceous chondrites and IDPs. Directly comparing H and N isotope analyses from chondrites is a daunting task, considering the various components (e.g., soluble and insoluble organics, organic grains and diffuse matter, phyllosilicates) and the multitude of techniques involved. In Fig. 17a, we plot δ^{15}N against δD values of bulk carbonaceous chondrites (Alexander et al., 2013), IDPs (Floss et al., 2006; Busemann et al., 2009; Davidson et al., 2012; Starkey and Franchi, 2013) and Isheyevo lithic clasts, as well as organic residues from carbonaceous and ordinary chondrites (Alexander et al., 2007). The bulk values from chondrites are obtained through digestion methods, whereas IDP and Isheyevo lithic clast data is obtained from *in situ* analyses, which likely results in an underestimation of bulk D/H values for these samples. From this data set, we can distinguish three groups: (1) ^{15}N-rich/D-depleted A- and H-clasts, (2) correlated ^{15}N-rich/D-rich IDPs, CR chondrites and the anomalous CM chondrite Bells and (3) very D-rich, but relatively ^{15}N-depleted IDPs and residues from ordinary and CR chondrites. CO, CV, CM and CI chondrites are all relatively depleted in ^{15}N and D and plot at the triple junction of these three groups. In Fig. 17b, we plot the inferred δ^{15}N–δD compositions of the organic endmembers from A- and H-clasts (large orange and blue circles, respectively) as implied from Section 4.1.1 and Fig. 16. We interpret these endmembers to be derived from ion-molecule reactions at different temperatures in the protostellar envelope, where the A-clast organic precursor formed at low temperatures (<10 K) on an isotope fractionation slope (grey array, Fig. 17b) consistent with Aléon (2010) and the H-clast precursor at higher temperatures (10 K $< T <$ 70 K, Millar et al., 1989) that is defined by a steep increase in D/H relative to ^{15}N (green array, Fig. 17b). Since bulk δ^{15}N–δD values are obtained from a mixture between these organic precursors and the isotope composition of the altering fluid, we can add mixing lines between the composition of the organic residues (squares in Fig. 17) and the bulk values of various Solar System objects and towards the fluid composition. We assume that the D/H ratio of the fluid endmember is fairly constant for most carbonaceous chondrites (Alexander et al., 2012) as well as for A- and H-clasts. The inferred D/H ratio of the CR water is proposed to be higher than other carbonaceous chondrites ($\delta D = +100‰$, Alexander et al., 2012), which would suggest a linear mixing line between CR IOM and the bulk. This in turn implies that the N-content of the fluid was very high for CR chondrites, as was previously suggested by Pizzarello et al. (2008) and Cobb et al. (2015) from their amino acid content. Indeed, the shape of the mixing lines in Fig. 17b depends on the elemental H/N ratio of the endmember components, which we calculate is at least an order of magnitude lower for the IOM (H/N = 0.5–3; Alexander et al., 2007) compared to the fluid depending on the amount of N added (H/N = 40 for 10% NH_3). While this is by no means an accurate determination

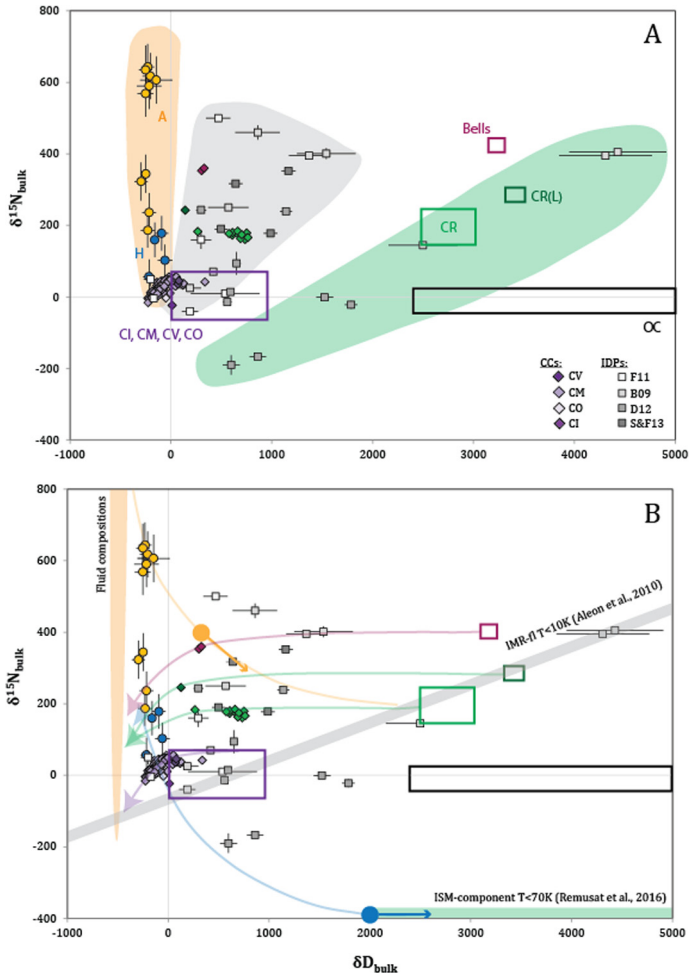

Fig. 17. (A) Summary plot of N versus H isotope data of bulk carbonaceous chondrites (diamonds, Alexander et al., 2013), IDPs (grey squares, Busemann et al., 2009; Davidson et al., 2012; Floss et al., 2006; Starkey and Franchi, 2013) and Isheyevo lithic clasts (yellow spheres: A-clasts; blue spheres: H-clasts) as well as the organic residues of carbonaceous chondrites (open squares, Alexander et al., 2007). Residue 'CR (L)' and corresponding bulk data is from anomalous CR chondrite LEW85332 Alexander et al., 2007 and 'Bells' is the anomalous CM chondrite Bells. The yellow, green and grey fields represent various H and N isotopic regions occupied by Solar System materials. We distinguish ^{15}N-rich/D-depleted (yellow), ^{15}N-rich/D-rich (grey) and very D-rich (green) isotopic regions. (B) Interpretation of data in panel A, where bulk H versus N isotope data represents a mixture between the composition of organic residues and an altering fluid that is variably enriched in ^{15}N and likely relatively constant in D/H, at least for chondrites Alexander et al., 2012. The composition of the organic precursors is established by isotope fractionation laws from Aléon (2010) (grey bar) and Remusat et al. (2016) (green bar) that exist in different temperature regimes in the ISM or protostellar envelope (see text for further explanation).

of the isotopic composition of the fluid, we conclude from Fig. 17 that primitive Solar System materials were affected by increasingly ^{15}N-rich fluids. We suggest that most carbonaceous chondrites (CV, CM, CO, CI) accreted an icy mixture relatively depleted in ^{15}N, whereas CR chondrites, CM chondrite Bells, H-clasts and A-clasts accreted more ^{15}N-rich N-bearing ices. Although the fluid endmember of the A-clasts is supposedly more ^{15}N-rich, it is likely that the organic precursor of these clasts is isotopically similar to CR chondrites. H-clasts on the other hand, have inherently different organic precursors that are isotopically similar to ordinary chondrites.

4.1.4. Nanoglobules as organic precursors?

Nanoglobules are ubiquitous in primitive Solar System objects such as chondrites (Garvie and Buseck, 2004) and perhaps also in comets (De Gregorio et al., 2010) and are considered as potential precursors to or sources of COM in meteorites. Their formation mechanisms are not fully understood and may include the genesis from icy dust grains in the ISM (Nakamura-Messenger et al., 2006; De Gregorio et al., 2010; De Gregorio et al., 2013) or formation during aqueous alteration processes on chondrite parent bodies (Dworkin et al., 2001). The ^{15}N and N/C composition of the globules found in A-clasts generally increase towards a ^{15}N-rich component that is similar to the diffuse OM and may represent the fluid composition (Fig. 16). It is, therefore, possible that the most unaltered globules in A-clasts represent the organic precursor material that is moderately ^{15}N–D rich (component b in Fig. 16 and 2 in Fig. 13). De Gregorio et al. (2013) show correlations between nanoglobule size, functional group

chemistry and meteorite hydration degree that identify the importance of increasing aqueous alteration on the growth of nanoglobules in CR and CM chondrites. Although nanoglobules may originally have an interstellar or disk heritage, subsequent growth of the globules apparently happens on the chondrite parent body during aqueous alteration. The nanoglobules in A-clasts are relatively small (~100 nm in diameter), even compared to the very pristine (unaltered) chondrite ALH 77307 De Gregorio et al., 2013), which suggests that A-clasts globules underwent only minor alteration. This is in agreement with the nm-sized phyllosilicates found in the hydrated veins of the A-clast FIB-sections that indicate limited growth during aqueous alteration (Fig. 3). Hence, the least altered nanoglobules in A-clasts may represent inherited OM from either the ISM or the disk and, thus, their structure and isotope composition can reflect the nature of these organic precursors.

The carbon structure of the seemingly unaltered A-clast nanoglobules (Fig. 8) differs most distinctly from other carbonaceous chondrites (CR, CM, CI spectra from Le Guillou et al. (2014)) by (1) a higher relative intensity of the C=O peak at 286.5 eV in the π^* transition and (2) a lower relative intensity of the COOH peak at 288.3 eV. From the more altered OM (Fig. 10), we observe a decrease of the intensity in the C=O peak. It has been suggested that the COOH peak contribution is related to the soluble component of the OM (Le Guillou et al., 2014) and, hence, the low contribution of this functional group to the A-clast nanoglobule structure may reflect their low degree of alteration. In addition, the diffuse OM observed in CI, CM and CR chondrites has a low contribution of C=O bonding environments. Therefore, if diffuse OM represents the soluble component as suggested by Le Guillou et al. (2014), then alteration of the initial OM can lower the C=O functionality in the organic precursor material. We note that the peak intensity at 286.5 eV may also in part be the result of increased C≡N functionality caused by radiation damage from the TEM similar to decomposition of amino acids measured by Zubavichus et al. (2004) and Hayabusa carbonaceous particles from Yabuta et al. (2014). However, in the latter case, the pre-TEM structure consisted of a relatively high intensity of C=O bonding to begin with. Moreover, De Gregorio et al. (2010) found a decrease in oxygenated functional groups post-TEM for cometary nanoglobules. In addition, these features are not observed in the H-clast structures, which were analyzed in a similar manner. Collectively, the observation of relatively high C=O and low COOH peak intensities confirms that the A-clast nanoglobules were altered to low degree and suggests that similar to cometary IDPs (Busemann et al., 2009), oxygen-rich bonding environments may have been important to the overall group functionality of A-clast organic precursor material. The H-clast carbon structure observed from clustered particles clearly has a lower peak contribution from C=O bonding environments relative to A-clast OM. We observe, however, no increase in aromaticity that is suggested to arise from progressive hydration as observed in CI and CM spectra (Le Guillou et al., 2014). In fact, we find no significant differences between A- and H-clasts when measuring the intensities of the 285 eV peaks relative to the 300 eV peaks in the carbon spectra. This could imply that the H-clast OM was initially less aromatic than A-clast OM, considering the significantly higher level of aqueous alteration in the H-clasts. However, this is rather speculative since variations in aromaticity determined by EELS can also be artificially produced by, for example, differences in the thickness of the FIB-sections.

4.1.5. Structure and isotope composition of altered OM: the fluid

From H and N isotope data, we have inferred the compositions of the fluids altering the H- and A-clast parent bodies. The D/H composition of both fluids is D-poor, to a similar degree as CO, CI and CM chondrites ($\delta D \approx -450‰$, Alexander et al., 2012), with the inferred A-clast fluid composition being more D-rich ($\delta D \approx -350‰$, Fig. 13, component 4) than the H-clast fluid ($\delta D \approx -450‰$, Fig. 13, component 3). The N isotope composition of the diffuse OM in both clast types appears similar (Fig. 16), but is likely an order of magnitude lower for the H-clasts (see Section 3.3 and Fig. 17). The H and N isotopic differences in the fluid compositions are accompanied by distinct variations in the N structures of more altered OM (Fig. 9). The A-clast OM has N–K edge functionality that we relate to N–heterocycles and nitrile bonding environments, whereas the H-clast OM is characterized by the absence of C–N bonding and the dominance of amine related functionality. Importantly, similar correlations between N group functionality and ^{15}N enrichments are found in chemical networks of simple N-bearing molecules in the ISM. HCN, NH_3 and isotopologues are relevant species to the ice composition of chondrites and comets, since these molecules can be stable in the Solar System at distances of <10 AU (Dodson-Robinson et al., 2009) and are abundant in the ISM as well as in comets (Ehrenfreund and Charnley, 2000; Mumma and Charnley, 2011). Theoretical models of interstellar isotope fractionation at low temperatures predict that N-bearing species such as HCN and NH_3 are enriched in ^{15}N and D to different degrees (Terzieva and Herbst, 2000; Rodgers and Charnley, 2008; Wirström et al., 2012). This is consistent with N isotope observations from several gaseous species in dense cores and protostellar environments that show ^{15}N enrichments in HCN and CN isotopologues comparable to that of A-clasts hotspots (Hily-Blant et al., 2013; Hily-Blant et al., 2013b; Wampfler et al., 2014). The level of ^{15}N enrichment observed for NH_3 is generally lower than predicted by models (Lis et al., 2010), which, in principle, may reflect the age of the dense core since later accreted monolayers of ammonia ice are expected to show ^{15}N enrichments similar to that observed in HCN and CN (Wirström et al., 2012). Moreover, $^{15}NH_2/^{14}NH_2$ ratios measured in cometary tails are as high as $^{15}N/^{14}N$ ratios measured in HCN and CN (Shinnaka et al., 2014), which suggests that a fractionation process could be operating in the protostellar stage that enhances ^{15}N in NH_3. Pizzarello and Bose (2015) proposed recombination of N_2 and H_2 condensates to NH_3 by UV irradiation as a possible mechanism to enrich NH_3 in ^{15}N, although this mechansim may only be relevant for cometary accretion regions. Collectively, we show that iso-

topical and structural variations in Isheyevo lithic clast OM have interesting parallels with NH_3 and HCN variations observed in the ISM. This implies that the compositional variations of the fluids that altered H- and A-clasts may reflect heterogeneous accretion of NH_3 and HCN derived species inherited from the ISM.

Finally, we briefly explore if the isotopic and structural signatures of diffuse OM provide insights into the origins of IOM and SOM. Diffuse OM in chondrites is associated with SOM by a higher intensity of carboxylic groups (Le Guillou et al., 2014) that is also recognized to be an important component in SOM (Pizzarello et al., 2006). Diffuse OM is typically interwoven with phyllosilicates in the hydrated regions of both H- and A-clasts. We can therefore consider SOM as an alteration product as well, introduced to the hydrated regions of chondrites by organic solvents in hydrothermal fluids. Alternatively, it has been suggested that SOM was extracted from IOM during aqueous alteration or that SOM formed in different temperature regimes than IOM from photo and thermochemical processes on ices in the ISM or protoplanetary disk (Ciesla and Sandford, 2012; De Marcellus et al., 2015; De Marcellus et al., 2017). Bulk SOM in CI and CM chondrites typically has higher $^{15}N/^{14}N$ and lower D/H ratios (Becker and Epstein, 1982) than bulk IOM from the same meteorites (Alexander et al., 2007), similar to our proposed isotope composition of the fluid (Fig. 17). This altering fluid, besides containing D-poor water, consists of ^{15}N-rich NH_3 and HCN that we propose accreted to different degrees as ices in chondrites. Relatively abundant ISM derived organic solvents such as formaldehyde and methanol could have reacted with these simple molecules and formed more complex soluble components that make up the SOM in chondrites. This line of reasoning suggests that IOM and SOM are both products of simple organic and inorganic molecules, which evolved through different channels: IOM is a product of photo and thermochemical processes on condensed ices (in different temperature regimes, see Section 4.1.3), whereas SOM evolved during aqueous alteration on chondrite parent bodies. Hence, SOM and IOM may have formed from similar compounds that were included to different extent and through different reactions, resulting in varying N and H isotopic signatures.

4.2. Implications for the accretion regions of chondrites

Our results establish that the two types of Isheyevo lithic clasts (A and H) incorporated two different organic precursors with distinct H and N isotope compositions and possibly carbon structures and subsequently experienced various degrees of fluid–rock interaction. These observations require that temporal and/or spatial variations in H and N isotopic compositions of organic matter must have existed in the accretion region of the clasts to account for their diverse organic heritage. We find that N isotope variations in the inferred fluid endmember compositions correlate with structural differences in the N bonding environments of their diffuse organic matter, in keeping with observations and models of NH_3 and HCN molecules in the ISM (Wirström et al., 2012; Hily-Blant et al., 2013; Hily-Blant et al., 2013b; Wampfler et al., 2014). In spite of these variations, the clasts and also CR chondrites belonging to the group of metal-rich carbonaceous chondrites have very similar bulk $^{26}Mg^*$–^{54}Cr signatures, suggesting a common accretion region distinct from other chondrites (Van Kooten et al., 2016). Our data indicate that ordinary chondrites and H-clasts that accreted at different times (Doyle et al., 2015; Van Kooten et al., 2016) incorporated similar D-rich and ^{15}N-poor organic precursor molecules. Likewise, CM, CI, CV and CO chondrites accreted similar D- and ^{15}N-rich organic precursors as CR chondrites and A-clasts. Ordinary chondrites appear to have accreted before carbonaceous chondrites (Doyle et al., 2015). Moreover, metal-rich carbonaceous chondrites accreted later than other chondrite groups (Krot et al., 2005; Bollard et al., 2015; Doyle et al., 2015; Schrader et al., 2017). Collectively, our results imply that the two organic precursors were present in distinct $^{26}Mg^*$–^{54}Cr reservoirs at different times, suggesting these isotope reservoirs were separated in both space and time. Nitrogen isotope variability in Solar System objects may be caused by temporal and spatial variations in chondrite accretion regions related to the relative positions of ice lines of N-bearing species. For example, earlier accretion of CM, CI, CV and CO chondrites in or near the asteroid belt (Alexander et al., 2012) could have resulted in the exclusion of N-bearing ices such as NH_3 and HCN and, subsequently, in a ^{15}N-depleted fluid. In contrast, later accretion of CR chondrites, H-clasts and A-clasts can result in progressive addition of these ices related to the inward movement of NH_3 and HCN ice stability regions with time (Dodson-Robinson et al., 2009). This is a side-effect of the disk cooling over time, primarily because of accretion onto the Sun depletes the disk of mass, which decreases the heat generated by disk turbulence. This is in agreement with a proposed higher abundance of ammonia in CR relative to CI/CM chondrites (Pizzarello et al., 2008; Cobb et al., 2015). Alternatively, metal-rich carbonaceous chondrites accreted at larger orbital distances. Based on bulk $^{26}Mg^*$ and ^{54}Cr, it is inferred that metal-rich chondrites and their components accreted in the outer Solar System, beyond the orbits of gas giants (Van Kooten et al., 2016). A possible mechanism to separate accretion regions is the formation of gas giants and the subsequent opening of gaps in the protoplanetary disk (Müller and Kley, 2013). According to the recently proposed Grand Tack model of the dynamical evolution of the early Solar System, the gas giants were not static but migrated sunwards during the lifetime of the protoplanetary disk and 'tacked' at 1.5 AU (Walsh et al., 2011). Excited during this inward-outward migration, some outer Solar System planetesimals were implanted into the main asteroid belt (Walsh et al., 2011). Hence, this migration may also account for some isotopic variability in the main asteroid belt. Finally, we emphasize that a complete understanding of the relationship between chondrite accretion regions and precursor molecules to complex organic matter requires a detailed knowledge of ^{15}N and D chemical networks, ice stability regions for N-bearing molecules and how these components evolve over time during the lifetime of the protoplanetary disk.

5. CONCLUSIONS

We report on the bulk N and H isotope compositions of Isheyevo lithic clasts and have investigated in detail the isotopic and structural nature of the complex organic matter by STEM-EELS and NanoSIMS. Our data provide the following constraints on the formation of OM in the Solar System:

(1) Isheyevo lithic clasts can be divided into two main types. Weakly hydrated clasts (A-clasts) consist of matrices dominated by Mg-rich olivines and pyroxenes and ^{15}N-rich, vein-like, hydrated regions with nm-sized phyllosilicates interwoven with diffuse OM and nanoglobules. Hydrated clasts (H-clasts) are dominated by a severely hydrated matrix consisting of larger phyllosilicates and secondary alteration products such as Fe-sulfides, magnetite, carbonates and clusters of carbonaceous matter with sulfides.

(2) The bulk H isotope data of H- and A-clasts are correlated with the degree of phyllosilicate hydration, but define two distinct populations. Since the D/H signature of the phyllosilicates represents a mixture of an organic and a fluid hydrogen component, we interpret this as evidence for the presence of multiple organic precursors and fluid compositions with approximately similar D/H signatures. The precursor of the H-clast OM is more D-rich than that of the A-clasts.

(3) The high resolution N isotope data of clast FIB-sections from ^{15}N-rich regions defined by SIMS show that the diffuse OM is on average more ^{15}N-rich than the nanoglobules. The most ^{15}N-rich regions ($\delta^{15}N < 5000‰$) are occupied by diffuse OM. We find by plotting δ^{15}N values of nanoglobules against their C/N ratio that the composition of the globules, similar to the H isotope data, is defined by multiple components. We suggest that the organic precursors of these nanoglobules are defined by a ^{15}N-poor (solar-like) component for H-clasts and a moderately ^{15}N-rich component for A-clasts.

(4) The least altered nanoglobules in A-clasts, represented by high C/N ratios and a lack of phyllosilicate overgrowth, might embody organic precursor material with moderately high D/H and $^{15}N/^{14}N$ ratios derived from the ISM. Their chemical structure is dissimilar to H-clast carbonaceous matter, which contains relatively lower contributions of C=O, CH_n and COOH bonding environments as well as a potentially lower initial aromaticity.

(5) Nitrogen structural information was obtained for more diffuse/altered OM interwoven with phyllosilicates and shows that ^{15}N-rich A-clasts contain nitrile-dominated functionality, whereas relatively ^{15}N-poor H-clasts are dominated by amine bonding environments. We suggest that, in line with observations and models of ISM N-bearing species, these correlations are related to heterogeneous accretion of HCN and NH_3 derived ices.

Similar to observations from Aléon (2010) and Remusat et al. (2016), our results suggest that the H isotope variability in bulk Solar System materials is largely controlled by heterogeneous accretion of at least two ISM-derived organic precursors (e.g., D-rich versus D- and ^{15}N-rich). Meanwhile, the N isotope variability is controlled by temporally and spatially displaced accretion of NH_3 and HCN containing ices to the altering fluid composition.

ACKNOWLEDGEMENT

This work was funded by grants from the Danish National Research Foundation (DNRF97) and from the European Research Council (ERC Consolidator grant agreement 616027-STARDUST2 ASTEROIDS) to M.B. J.K.J. acknowledges support from a Lundbeck Foundation Group Leader Fellowship as well as the European Research Council (ERC) under the European Union's Horizon 2020 research and innovation programme (grant agreement No 646908) through ERC Consolidator Grant "S4F".

APPENDIX A. SUPPLEMENTARY DATA

Supplementary data associated with this article can be found, in the online version, at http://dx.doi.org/10.1016/j.gca.2017.02.002.

REFERENCES

Alexander C., Newsome S., Fogel M., Nittler L., Busemann H. and Cody G. (2010) Deuterium enrichments in chondritic macromolecular material – implications for the origin and evolution of organics, water and asteroids. *Geochim. Cosmochim. Acta* **74**, 4417–4437.

Alexander C. M. O., Bowden R., Fogel M. L., Howard K. T., Herd C. D. K. and Nittler L. R. (2012) The Provenances of asteroids, and their contributions to the volatile inventories of the terrestrial planets. *Science* **337**, 721–723.

Alexander C. M. O., Fogel M., Yabuta H. and Cody G. D. (2007) The origin and evolution of chondrites recorded in the elemental and isotopic compositions of their macromolecular organic matter. *Geochim. Cosmochim. Acta* **71**, 4380–4403.

Alexander C. M. O., Howard K. T., Bowden R. and Fogel M. L. (2013) The classification of CM and CR chondrites using bulk H, C and N abundances and isotopic compositions. *Geochim. Cosmochim. Acta* **123**, 244–260.

Aléon J. (2010) Multiple origins of nitrogen isotopic anomalies in meteorites and comets. *Astrophys. J.* **722**, 1342.

Alt J. and Shanks W. (2006) Stable isotope compositions of serpentine seamounts in the mariana forearc: serpentization processes, fluid sources and sulfur metasomatism. *Earth Planet. Sci. Lett.* **242**, 272–285.

Altwegg K., Balsiger H., Bar-Nun A., Berthelier J. J., Bieler A., Bochsler P., Briois C., Calmonte U., Combi M., Keyser J. D., Eberhardt P., Fiethe B., Fuselier S., Gasc S., Gombosi T. I., Hansen K. C., Hässig M., Jäckel A., Kopp E., Korth A., LeRoy L., Mall U., Marty B., Mousis O., Neefs E., Owen T., Réme H., Rubin M., Sémon T., Tzou C.-Y., Waite H. and Wurz P. (2015) 67P/Churyumov-Gerasimenko, a Jupiter family comet with a high D/H ratio. *Science* **347**, 1261952.

Becker R. and Epstein S. (1982) Carbon, hydrogen and nitrogen isotopes from solvent-extractable organic matter in carbonaceous chondrites. *Geochim. Cosmochim. Acta* **46**, 97–103.

Belloche A., Garrod R. T., Müller H. S. P. and Menten K. M. (2014) Detection of a branched alkyl molecule in the interstellar medium: iso-propyl cyanide. *Science* **345**, 1584–1587.

Bergin E. A., Blake G. A., Ciesla F., Hirschmann M. M. and Li J. (2015) Tracing the ingredients for a habitable earth from interstellar space through planet formation. *Proc. Natl. Acad. Sci.* **112**, 8965–8970.

Biver N., Bockelée-Morvan D., Moreno R., Crovisier J., Colom P., Lis D. C., Sandqvist A., Boissier J., Despois D. and Milam S. N. (2015) Ethyl alcohol and sugar in comet C/2014 Q2 (Lovejoy). *Sci. Adv.* **1**, e1500863.

Bizzarro M., Paton C., Larsen K., Schiller M., Trinquier A. and Ulfbeck D. (2011) High-precision Mg-isotope measurements of terrestrial and extraterrestrial material by HR-MC-ICPMS—implications for the relative and absolute Mg-isotope composition of the bulk silicate Earth. *J. Anal. At. Spectrom.* **26**, 565–577.

Bockelée-Morvan D., Calmonte U., Charnley S., Duprat J., Engrand C., Gicquel A., Hässig M., Jehin E., Kawakita H., Marty B., Milam S., Morse A., Rousselot P., Sheridan S. and Wirström E. (2015) Cometary isotopic measurements. *Space Sci. Rev.* **197**, 47–83.

Bollard J., Connelly J. N. and Bizzarro M. (2015) Pb-Pb dating of individual chondrules from the CBa chondrite Gujba: assessment of the impact plume formation model. *Meteorit. Planet. Sci.* **50**, 1197–1216.

Bonal L., Huss G., Krot A., Nagashima K., Ishii H. and Bradley J. (2010a) Highly 15N-enriched chondritic clasts in the CB/CH-like meteorite Isheyevo. *Geochim. Cosmochim. Acta* **74**, 2011–2016.

Bonal L., Huss G. R., Krot A. N. and Nagashima K. (2010b) Chondritic lithic clasts in the CB/CH-like meteorite Isheyevo: Fragments of previously unsampled parent bodies. *Geochim. Cosmochim. Acta* **74**, 2500–2522.

Briani G., Gounelle M., Marrocchi Y., Mostefaoui S., Leroux H., Quirico E. and Meibom A. (2009) Pristine extraterrestrial material with unprecedented nitrogen isotopic variation. *Proc. Natl. Acad. Sci. U.S.A.* **106**, 10522–10527.

Brownlee D., Joswiak D. and Matrajt G. (2012) Overview of the rocky component of Wild 2 comet samples: insight into the early solar system, relationship with meteoritic materials and the differences between comets and asteroids. *Meteorit. Planet. Sci.* **47**, 453–470.

Bunch T. and Chang S. (1980) Carbonaceous chondrite-II. Carbonaceous chondrite phyllosilicates and light element geochemistry as indicators of parent body processes and surface conditions. *Geochim. Cosmochim. Acta* **44**, 1543–1577.

Busemann H., Alexander C. M. O., Nittler L. R., Zega T. J., Stroud R. M., Bajt S., Cody G. D., and Yabuta, H., 2006. Correlated analyses of D- and 15N-rich carbon grains from CR2 chondrite EET 92042.

Busemann H., Nguyen A. N., Cody G. D., Hoppe P., Kilcoyne A. L. D., Stroud R. M., Zega T. J. and Nittler L. R. (2009) Ultraprimitive interplanetary dust particles from the comet 26P/Grigg–Skjellerup dust stream collection. *Earth. Planet. Sci. Lett.* **288**, 44–57.

Chakraborty S., Muskatel B. H., Jackson T. L., Ahmed M., Levine R. D. and Thiemens M. H. (2014) Massive isotopic effect in vacuum UV photodissociation of N_2 and implications for meteorite data. *Proc. Natl. Acad. Sci. U.S.A.* **111**, 14704–14709.

Ciesla F. and Sandford S. (2012) Organic synthesis via irradiation and warming of ice grains in the solar nebula. *Science* **336**, 452–454.

Clayton R. (2002) Solar system: self-shielding in the solar nebula. *Nature* **415**, 860–861.

Cleeves L. I., Bergin E. A., Alexander C. M. O., Du F., Graninger D., Öberg K. I. and Harries T. J. (2014) The ancient heritage of water ice in the solar system. *Science* **345**, 1590–1593.

Cleeves L. I., Bergin E. A., Alexander C. M. O., Du F., Graninger D., Öberg K. I. and Harries T. J. (2016) Exploring the origins of deuterium enrichments in solar nebular organics. *Astrophys. J.* **819**, 13.

Coakley K. J., Simons D. S. and Leifer A. M. (2005) Secondary ion mass spectrometry measurements of isotopic ratios: correction for time varying count rate. *Int. J. Mass Spectrom.* **240**, 107–120.

Cobb A. K., Pudritz R. E. and Pearce B. K. D. (2015) Nature's starships II: Simulating the synthesis of amino acids in meteorite parent bodies. *Astrophys. J.* **809**, 6.

Cody G. D., Ade H., Alexander C. M. O., Araki T., Butterworth A., Fleckenstein H., Flynn G., Gilles M. K., Jacobsen C., Kilcoyne A. L. D., Messenger K., Sandford S. A., Tyliszczak T., Westphal A. J., Wirick S. and Yabuta H. (2008) Quantitative organic and light-element analysis of comet 81P/Wild 2 particles using C-, N-, and O-μ-XANES. *Meteorit. Planet. Sci. Archiv.* **43**, 353–365.

Cody G. D., Heying E., Alexander C. M. O., Nittler L. R., Kilcoyne A. L. D., Sandford S. A. and Stroud R. M. (2011) Establishing a molecular relationship between chondritic and cometary organic solids. *Proc. Natl. Acad. Sci. U.S.A.* **108**, 19171–19176.

Cooper G., Kimmich N., Belisle W., Sarinana J., Brabham K. and Garrel L. (2001) Carbonaceous meteorites as a source of sugar-related organic compounds for the early Earth. *Nature* **414**, 879–883.

Davidson J., Busemann H. and Franchi I. A. (2012) A NanoSIMS and Raman spectroscopic comparison of interplanetary dust particles from comet Grigg-Skjellerup and non-Grigg Skjellerup collections. *Meteorit. Planet. Sci.* **47**, 1748–1771.

De Gregorio B. T., Stroud R. M., Nittler L. R., Alexander C. M. O., Bassim N. D., Cody G. D., Kilcoyne A. L. D., Sandford S. A., Milam S. N., Nuevo M. and Zega T. J. (2013) Isotopic and chemical variation of organic nanoglobules in primitive meteorites. *Meteorit. Planet. Sci.* **48**, 904–928.

De Gregorio B. T., Stroud R. M., Nittler L. R., Alexander C. M. O., Kilcoyne A. L. D. and Zega T. J. (2010) Isotopic anomalies in organic nanoglobules from comet 81P/Wild 2: Comparison to Murchison nanoglobules and isotopic anomalies induced in terrestrial organics by electron irradiation. *Geochim. Cosmochim. Acta* **74**, 4454–4470.

De Marcellus P., Fresneau A., Brunetto R., Danger G., Duvernay F., Meinert C., Meierhenrich U., Borondics F., Chiavassa T. and d'Hendecourt L. (2017) Photo and thermochemical evolution of astrophysical ice analogues as a source for soluble and insoluble organic materials in solar system minor bodies. *Mon. Not. Roy. Astron. Soc.* **464**, 114–120.

De Marcellus P., Meinert C., Myrgorodska I., Nahon L., Buhse T., d'Hendecourt L. and Meierhenrich U. (2015) Aldehydes and sugars from evolved precometary ice analogs: Importance of ices in astrochemical and prebiotic evolution. *Proc. Natl. Acad. Sci. U.S.A.* **112**, 965–970.

Deloule E. and Robert F. (1995) Interstellar water in meteorites? *Geochim. Cosmochim. Acta* **59**, 4695–4705.

Dodson-Robinson S. E., Willacy K., Bodenheimer P., Turner N. J. and Beichman C. A. (2009) Ice lines, planetesimal composition and solid surface density in the solar nebula. *Icarus* **200**, 672–693.

Doyle P. M., Jogo K., Nagashima K., Krot A., Wakita S., Ciesla F. J. and Hutcheon I. D. (2015) Early aqueous activity on the ordinary and carbonaceous chondrite parent bodies recorded by fayalite. *Nat. Commun.* **6**, 7444.

Dworkin J., Deamer D., Sandford S. and Allamandola L. (2001) Self-assembling amphiphilic molecules: Synthesis in simulated interstellar/precometary ices. *Proc. Natl. Acad. Sci. U.S.A.* **98**, 815–819.

Ehrenfreund P. and Charnley S. B. (2000) Organic Molecules in the Interstellar Medium, Comets, and Meteorites: A Voyage from Dark Clouds to the Early Earth. *Ann. Rev. Astron. Astrophys.* **38**, 427–483.

Fitzsimons I., Harte B. and Clark R. (2000) SIMS stable isotope measurement: counting statistics and analytical precision. *Min. Mag.* **64**, 59–83.

Floss C., Stadermann F. J., Bradley J. P., Dai Z. R., Bajt S., Graham G. and Lea A. S. (2006) Identification of isotopically primitive interplanetary dust particles: a NanoSIMS isotopic imaging study. *Geochim. Cosmochim. Acta* **70**, 2371–2399.

Franke R., Bender S. and Hormes J. (1995) N K-shell absorption spectra of ionic and molecular crystals. *Phys. B* **208**, 293–294.

Garenne A., Beck P., Montes-Hernandez G., Chiriac R., Toche F., Quirico E., Bonal L. and Schmitt B. (2014) The abundance and stability of water in type 1 and 2 carbonaceous chondrites (CI, CM and CR). *Geochim. Cosmochim. Acta* **137**, 93–112.

Garvie L. and Buseck P. (2004) Nanosized carbon-rich grains in carbonaceous chondrite meteorites. *Earth Planet. Sci. Lett.* **224**, 431–439.

Grady M. M. and Wright I. P. (2003) Elemental and isotopic abundances of carbon and nitrogen in meteorites. *Space Sci. Rev.* **106**, 231–248.

Hartogh P., Lis D. C., Bockelée-Morvan D., de Val-Borro M., Biver N., Küppers M., Emprechtinger M., Bergin E. A., Crovisier J., Rengel M., Moreno R., Szutowicz S. and Blake G. A. (2011) Ocean-like water in the Jupiter-family comet 103P/Hartley 2. *Nature* **478**, 218–220.

Heays A. N., Visser R., Gredel R., Ubachs W., Lewis B. R., Gibson S. T. and van Dishoeck E. F. (2014) Isotope selective photodissociation of N_2 by the interstellar radiation field and cosmic rays. *Astron. Astrophys.* **562**, A61.

Herbst E. and Dishoeck E. F. v. (2009) Complex organic interstellar molecules. *Ann. Rev. Astron. Astrophys.* **47**, 427–480.

Hily-Blant P., Bonal L., Faure A. and Quirico E. (2013) The ^{15}N-enrichment in dark clouds and Solar System objects. *Icarus* **223**, 582–590.

Hily-Blant P., Pineau des Forêts G., Faure A., Le Gal R. and Padovani M. (2013b) The CN/C ^{15}N isotopic ratio towards dark clouds. *Astron. Astrophys.* **557**, A65.

Huss G., Nagashima K., Burnett D., Jurewicz A., and Olinger C., 2012. A new upper limit on the D/H ratio in the solar wind. In: *43rd Lunar and Planetary Science Conference* 43, p. 1709.

Injerd W. G. and Kaplan I. R. (1974) Nitrogen isotope distribution in meteorites. *Meteoritics* **9**, 352.

Iqbal M. Z., Katsiotis M. S., Alhassan S. M., Liberatore M. W. and Abdala A. A. (2014) Effect of solvent on the uncatalyzed synthesis of aminosilane-functionalized graphene. *RSC Adv.* **4**, 6830–6839.

Ishii H., Bradley J., Bonal L., Krot A., Nagashima K. and Huss G. (2009) Nitrogen carrier identified in 15N extreme hotspots in the isheyevo (CH/CB) meteorite. *Ann. Met. Soc. Meeting* **73**, 5406.

Ivanova M. A., Kononkova N. N., Krot A. N., Greenwood R. C., Franchi I. A., Verchovsky A. B., Trieloff M., Korochantseva E. V. and Brandstätter F. (2008) The Isheyevo meteorite: mineralogy, petrology, bulk chemistry, oxygen, nitrogen, carbon isotopic compositions, and ^{40}Ar-^{39}Ar ages. *Meteorit. Planet. Sci.* **43**, 915–940.

Jørgensen J. K., Favre C., Bisschop S. E., Bourke T. L., van Dishoeck E. F. and Schmalzl M. (2012) Detection of the simplest sugar, glycolaldehyde, in a solar-type protostar with ALMA. *Astrophys. J.* **757**, L4.

Kebukawa Y., Kilcoyne A. L. D. and Cody G. D. (2013) Exploring the potential formation of organic solids in chondrites and comets through polymerization of interstellar formaldehyde. *Astrophys. J.* **771**, 19.

Keller L. P., Messenger S., Flynn G. J., Clemett S., Wirick S. and Jacobsen C. (2004) The nature of molecular cloud material in interplanetary dust. *Geochim. Cosmochim. Acta* **68**, 2577–2589.

Kerridge J. F. (1985) Carbon, hydrogen and nitrogen in carbonaceous chondrites: abundances and isotopic compositions in bulk samples. *Geochim. Cosmochim. Acta* **49**, 1707–1714.

King A., Solomon J., Schofield P. and Russell S. (2015) Characterising the CI and CI-like carbonaceous chondrites using thermogravimetric analysis and infrared spectroscopy. *Earth Planet. Space* **67**, 198.

Krot A. N., Amelin Y., Cassen P. and Meibom A. (2005) Young chondrules in CB chondrites from a giant impact in the early Solar System. *Nature* **436**, 989–992.

Kuga M., Marty B., Marrocchi Y. and Tissandier L. (2015) Synthesis of refractory organic matter in the ionized gas phase of the solar nebula. *Proc. Natl. Acad. Sci. U.S.A.* **112**, 7129–7134.

Lajaunie L., Boucher F., Dessapt R. and Moreau P. (2015) Quantitative use of electron energy-loss spectroscopy Mo-$M_{2,3}$ edges for the study of molybdenum oxides. *Ultramicroscopy* **149**, 1–8.

Larsen K. K., Trinquier A., Paton C., Schiller M., Wielandt D., Ivanova M. A., Connelly J. N., Nordlund A., Krot A. N. and Bizzarro M. (2011) Evidence for Magnesium Isotope Heterogeneity in the Solar Protoplanetary Disk. *Astrophys. J.* **735**, L37.

Laurent B., Roskosz M., Remusat L., Robert F., Leroux H., Vezin H., Depecker C., Nuns N. and Lefebvre J.-M. (2015) The deuterium/hydrogen distribution in chondritic organic matter attests to early ionizing irradiation. *Nat. Commun.* **6**, 8567.

Le Guillou C., Bernard S., Brearley A. J. and Remusat L. (2014) Evolution of organic matter in Orgueil, Murchison and Renazzo during parent body aqueous alteration: In situ investigations. *Geochim. Cosmochim. Acta* **131**, 368–392.

Lis D. C., Wootten A., Gerin M. and Roueff E. (2010) Nitrogen isotopic fractionation in interstellar ammonia. *Astrophys. J.* **710**, L49.

Lyons J. (2009) N_2 self-shielding in the solar nebula. *Ann. Met. Soc.* **72**, 5437.

Marty B., Kelley S. and Turner G. (2010a) Chronology and shock history of the Bencubbin meteorite: a nitrogen, noble gas, and Ar–Ar investigation of silicates, metal and fluid inclusions. *Geochim. Cosmochim. Acta* **74**, 6636–6653.

Marty B., Zimmerman L., Burnard P., Wieler R., Heber V., Burnett D., Wiens R. and Bochsler P. (2010b) Nitrogen isotopes in the recent solar wind from the analysis of genesis targets: Evidence for large scale isotope heterogeneity in the early solar system. *Geochim. Cosmochim. Acta* **74**, 340–355.

Messenger S. (2000) Identification of molecular-cloud material in interplanetary dust particles. *Nature* **404**, 968–971.

Millar T. J., Bennett A. and Herbst E. (1989) Deuterium fractionation in dense interstellar clouds. *Astrophys. J.* **340**, 906–920.

Müller T. and Kley W. (2013) Modelling accretion in transitional disks. *Astron. Astrophys.* **560**, A40.

Mumma M. J. and Charnley S. B. (2011) The chemical composition of comets—emerging taxonomies and natal heritage. *Ann. Rev. Astron. Astrophys.* **49**, 471–524.

Nakamura-Messenger K., Messenger S., Keller L. P., Clemett S. J. and Zolensky M. E. (2006) Organic globules in the Tagish Lake

meteorite: remnants of the protosolar disk. *Science* **314**, 1439–1442.

Paton C., Hellstrom J., Paul B., Woodhead J. and Hergt J. (2011) Iolite: Freeware for the visualisation and processing of mass spectrometric data. *J. Anal. At. Spectrom.* **26**, 2508–2518.

Piani L., Remusat L. and Robert F. (2012) Determination of the H isotopic composition of individual components in fine-scale mixtures of organic matter and phyllosilicates with the nanoscale secondary ion mass spectrometry. *Anal. Chem.* **84**, 10199–10206.

Pizzarello S. and Bose M. (2015) The path of reduced nitrogen toward early Earth: the cosmic trail and its solar shortcuts. *Astrophys. J.* **814**, 107–114.

Pizzarello S., Cooper G. and Flynn G. (2006) The nature and distribution of the organic material in carbonaceous chondrites and interplanetary dust particles. *Meteor. Early Solar Syst. II* **943**, 625–651.

Pizzarello S., Huang Y. and Alexandre M. R. (2008) Molecular asymmetry in extraterrestrial chemistry: Insights from a pristine meteorite. *Proc. Natl. Acad. Sci. U.S.A.* **105**, 3700–3704.

Remusat L., Palhol F., Robert F., Derenne S. and France-Lanord C. (2006) Enrichment of deuterium in insoluble organic matter from primitive meteorites: A solar system origin? Earth Planet. *Sci. Lett.* **243**, 15–25.

Remusat L., Piani L. and Bernard S. (2016) Thermal recalcitrance of the organic D-rich component of ordinary chondrites. *Earth Planet. Sci. Lett.* **435**, 36–44.

Remusat L., Robert F., Meibom A., Mostefaoui S., Delpoux O., Binet L., Gourier Didie and Derenne S. (2009) Proto-planetary disk chemistry recorded by D-rich organic radicals in carbonaceous chondrites. *Astrophys. J.* **698**, 2087.

Robert F. and Epstein S. (1982) The concentration and isotopic composition of hydrogen, carbon and nitrogen in carbonaceous meteorites. *Geochim. Cosmochim. Acta* **46**, 81–95.

Rodgers S. D. and Charnley S. B. (2008) Nitrogen superfractionation in dense cloud cores. *Mon. Not. Roy. Astron. Soc. Lett.* **385**, L48–L52.

Roueff E., Loison J. and Hickson K. (2015) Isotopic fractionation of carbon, deuterium, and nitrogen: a full chemical study. *Astron. Astrophys.* **576**, A99.

Schrader D., Nagashima K., Krot A. N., Ogliore R., Yin Q.-Z., Amelin Y., Stirling C. and Kaltenbach A. (2017) Distribution of ^{26}Al in the CR chondrite chondrule-forming region of the protoplanetary disk. *Geochim. Cosmochim. Acta* **201**, 275–302.

Shinnaka Y., Kawakita H., Kobayashi H., Nagashima M. and Boice D. C. (2014) $^{14}NH_2/^{15}NH_2$ Ratio in Comet C/2012 S1 (ISON) Observed during its Outburst in 2013 November. *Astrophys. J.* **782**, L16.

Starkey N. A. and Franchi I. A. (2013) Insight into the silicate and organic reservoirs of the comet forming region. *Geochim. Cosmochim. Acta* **105**, 73–91.

Terzieva R. and Herbst E. (2000) The possibility of nitrogen isotopic fractionation in interstellar clouds. *Mon. Not. Roy. Astron. Soc.* **317**, 563–568.

Tomeoka K. and Buseck P. (1988) Matrix mineralogy of the Orgueil CI carbonaceous chondrite. *Geochim. Cosmochim. Acta* **52**, 1627–1640.

Van Kooten E. M. M. E., Wielandt D., Schiller M., Nagashima K., Thomen A., Larsen K. K., Olsen M. B., Nordlund k., Krot A. N. and Bizzarro M. (2016) Isotopic evidence for primordial molecular cloud material in metal-rich carbonaceous chondrites. *Proc. Natl. Acad. Sci.* **113**, 2011–2016.

Vollmer C., Kepaptsoglou D., Leitner J., Busemann H., Spring N. H., Ramasse Q. M., Hoppe P. and Nittler L. R. (2014) Fluid-induced organic synthesis in the solar nebula recorded in extraterrestrial dust from meteorites. *Proc. Natl. Acad. Sci. U.S. A.* **111**, 15338–15343.

Walsh K., Morbidelli A., Raymond S., O'Brien D. and Mandell A. (2011) A low mass for Mars from Jupiter's early gas-driven migration. *Nature* **475**, 206–209.

Wampfler S. F., Jorgensen J. K., Bizzarro M. and Bisschop S. E. (2014) Observations of nitrogen isotope fractionation in deeply embedded protostars. *Astron. Astrophys.* **572**, A24.

Wasson J. T. and Rubin A. E. (2010) Metal in CR chondrites. *Geochim. Cosmochim. Acta* **74**, 2212–2230.

Weisberg M., Prinz M., Clayton R. and Mayeda T. (1993) The CR (Renazzo-type) carbonaceous chondrite group and its implications. *Geochim. Cosmochim. Acta* **57**, 1576–1586.

Wirström E. S., Charnley S. B., Cordiner M. A. and Milam S. N. (2012) Isotopic anomalies in primitive solar system matter: Spin-state dependent fractionation of nitrogen and deuterium in interstellar clouds. *Astrophys. J.* **757**, L11.

Yabuta H., Uesugi M., Naraoka H., Ito M., Kilcoyne A. L. D., Sandford S. A., Kitajima F., Mita H., Takano Y., Yada T., Karouji Y., Ishibashi Y., Okada T. and Abe M. (2014) X-ray absorption near edge structure spectroscopic study of Hayabusa category 3 carbonaceous particles. *Earth Planet. Space* **66**, 156.

Yang L., Ciesla F. J. and Alexander C. M. O. (2013) The D/H ratio of water in the solar nebula during its formation and evolution. *Icarus* **226**, 256–267.

Zega T. J., Alexander C. M. O., Busemann H., Nittler L. R., Hoppe P., Stroud R. M. and Young A. F. (2010) Mineral associations and character of isotopically anomalous organic material in the Tagish Lake carbonaceous chondrite. *Geochim. Cosmochim. Acta* **74**, 5966–5983.

Zubavichus Y., Fuchs O., Weinhardt L., Heske C., Umbach E., Denlinger J. D. and Grunze M. (2004) Soft X-ray-induced decomposition of amino acids: an XPS, mass spectrometry, and NEXAFS study. *Rad. Res.* **161**, 346–358.

Associate editor: Eric Quirico